RESEARCH ARTICLE SUMMARY

MICROBIOLOGY

Mechanism of bacterial predation via ixotrophy

Yun-Wei Lien, Davide Amendola, Kang Soo Lee, Nina Bartlau, Jingwei Xu, Go Furusawa, Martin F. Polz, Roman Stocker, Gregor L. Weiss*, Martin Pilhofer*

INTRODUCTION: Freshwater and ocean habitats are heterogeneous environments where nutrient concentrations fluctuate across space and time. Ixotrophy has been proposed as a predatory strategy for bacterial strains within the phylum *Bacteroidota* to access substrate that is bound in living microbes. Known ixotrophic bacteria are filamentous, and—just like flypaper—they catch prey cells and stick them to their cell surface. Flagella of prey cells have been reported to play a role in this catching behavior, which is followed by prey cell lysis. Some ixotrophic predators contain rod-shaped particles, called "rhapidosomes." These share structural similarities with contractile injection systems (CISs), which are macromolecular injection devices known to mediate bacterial antagonism.

RATIONALE: The molecular mechanism of ixotrophy remains poorly understood. In this study, we set out to address the following questions: (i) How is the prey caught? (ii) How is the prey killed? (iii) How is the activity of ixotrophy toggled? (iv) Why do cells use ixotrophy?

RESULTS: We used *Aureispira* sp. CCB-QB1 as a model to characterize ixotrophy both in liquid and on solid medium, employing killing assays against *Vibrio campbellii* as prey. In both environments, ixotrophy was observed as a two-step process: (i) The predator establishes contact with prey cells, either by immobilizing them on its cell surface (in liquid medium) or by approaching them using gliding motility (on solid surface), and (ii) the predator kills the prey in a contact-dependent manner. To observe ultrastructures that may be involved in this predatory behavior, we imaged a predator-prey mixture by cryo–electron tomography. The tomograms showed that every *Aureispira* cell had extracellular rods with terminal "grappling hooks," which interacted with prey cell flagella. Single-particle cryo–electron microscopy identified these grappling hooks as heptamers of a type IX secretion system (T9SS) substrate. Additionally, *Aureispira* exhibited multiple type VI secretion systems (T6SSs), a class of CISs that are anchored in the cell envelope. These T6SSs had an elaborate transenvelope complex and an extracellular antenna. Upon contract T6SSs were seen to expel their inner tube puncture the prey cell. Single-cell Raman microspectroscopy with stable isotope–labeled prey demonstrated that prey components are taken up by the attacker. Furthermore, nutrient availability affected the activity of ixotrophy through insertion sequences (ISs) that provide genetic variation for selection. Under nutrient-rich conditions, ISs were found to insert into ixotrophy-related genes, deactivating their expression. In nutrient-limiting conditions, we observed reactivation events by IS excisions, leading to a fitness advantage through resumed ixotrophy.

CONCLUSION: We provide an integrative model for bacterial ixotrophy that involves the interplay of multiple cellular machineries. The presence of gene clusters encoding these machineries in other ixotrophy-positive bacteria indicates a conserved molecular mechanism. Ixotrophy may play an overlooked but critical role for bacteria to access nutrients in heterogeneous aquatic environments and in shaping microbial populations. ■

The list of author affiliations is available in the full article online.
*Corresponding author. Email: pilhofer@biol.ethz.ch (M.P.); gregor.weiss@mol.biol.ethz.ch (G.L.W.)
Cite this article as Y.-W. Lien *et al.*, *Science* **386**, eadp0614 (2024). DOI: 10.1126/science.adp0614

READ THE FULL ARTICLE AT
https://doi.org/10.1126/science.adp0614

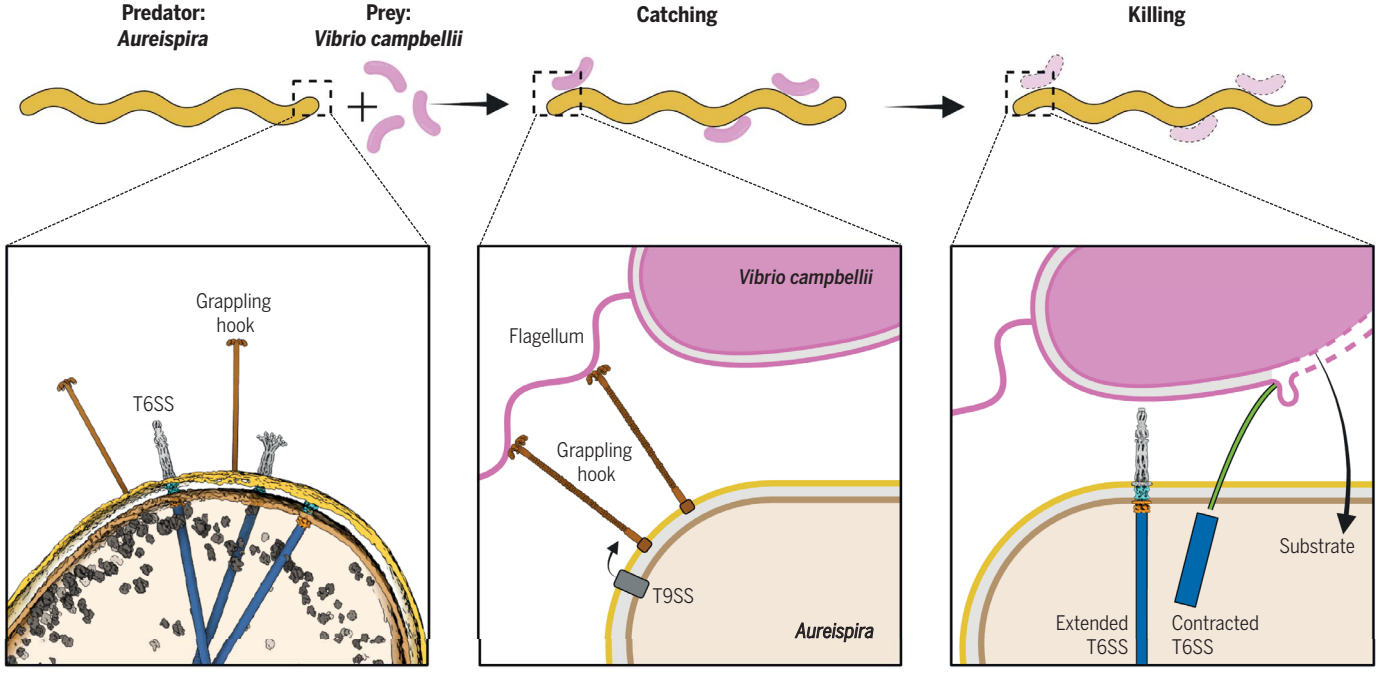

Mechanism of bacterial predation through ixotrophy. *Aureispira* predates through a two-step process: Cell-cell contact with prey is established using gliding motility (on solid surfaces) or T9SS-secreted grappling hooks (in liquid environments). This is followed by prey killing by means of a T6SS and uptake of substrates. [Figure partly created with BioRender.com]

RESEARCH ARTICLE

MICROBIOLOGY

Mechanism of bacterial predation via ixotrophy

Yun-Wei Lien[1], Davide Amendola[1], Kang Soo Lee[2]†, Nina Bartlau[3], Jingwei Xu[1], Go Furusawa[4], Martin F. Polz[3], Roman Stocker[2], Gregor L. Weiss[1]*, Martin Pilhofer[1]*

Ixotrophy is a contact-dependent predatory strategy of filamentous bacteria in aquatic environments for which the molecular mechanism remains unknown. We show that predator-prey contact can be established by gliding motility or extracellular assemblages we call "grappling hooks." Cryo–electron microscopy identified the grappling hooks as heptamers of a type IX secretion system substrate. After close predator-prey contact is established, cryo–electron tomography and functional assays showed that puncturing by a type VI secretion system mediated killing. Single-cell analyses with stable isotope–labeled prey revealed that prey components are taken up by the attacker. Depending on nutrient availability, insertion sequence elements toggle the activity of ixotrophy. A marine metagenomic time series shows coupled dynamics of ixotrophic bacteria and prey. We found that the mechanism of ixotrophy involves multiple cellular machineries, is conserved, and may shape microbial populations in the environment.

Freshwater and ocean habitats are often heterogeneous environments with nutrient concentrations varying drastically across space and time (*1*, *2*). Predation is a strategy for bacteria to access substrate that is bound in living microbes. The number of known bacterial predatory mechanisms is surprisingly low—specific examples have been observed in *Myxococcus xanthus*, *Bdellovibrio*-like organisms, *Candidatus* Uabimicrobium amorphum, and *Vampirococcus* species (*3*–*7*).

Ixotrophy has previously been proposed as a widespread facultative predatory strategy for strains of the phylum *Bacteroidota* (*8*, *9*), and supplementation with the prey cells can be sufficient for ixotrophic bacteria to grow. Known ixotrophic bacteria are filamentous and multicellular, and—just like flypaper—they catch prey cells and stick them to their cell surface, followed by prey lysis. Known prey cells range from diverse bacterial species such as *Vibrio*, *Photobacterium*, and various cyanobacterial strains (e.g., *Anabaena*, *Synechocystis*, *Synechococcus*, *Microcystis*) to eukaryotic organisms, such as diatoms (*8*–*13*). A given ixotrophic predator typically shows specificity toward a subset of prey cells. Although prey flagella have been reported to play a crucial role in ixotrophy, the underlying mechanisms of specificity, catching, and killing are not well understood.

[1]Institute of Molecular Biology and Biophysics, Department of Biology, ETH Zürich, 8093 Zürich, Switzerland. [2]Institute of Environmental Engineering, Department of Civil, Environmental and Geomatic Engineering, ETH Zürich, 8093 Zürich, Switzerland. [3]Division of Microbial Ecology, Centre for Microbiology and Environmental Systems Science, University of Vienna, 1030 Vienna, Austria. [4]Centre for Chemical Biology, Universiti Sains Malaysia, 11900 Bayan Lepas, Malaysia.
***Corresponding author. Email: pilhofer@biol.ethz.ch (M.P.); gregor.weiss@mol.biol.ethz.ch (G.L.W.)**
†Present address: Department of Mechanical Engineering, Ulsan National Institute of Science and Technology (UNIST), Ulsan 44919, South Korea.

Some ixotrophy-positive strains contain intriguing rod-shaped particles, called "rhapidosomes" (*14*, *15*), which were speculated to be involved in gliding motility. It was shown that these structures comprise a protein with similarities to a contractile injection system (CIS) from *Serratia entomophila* (*16*). Notably, CISs from other microorganisms have been shown to mediate diverse cell-cell interactions (*17*–*22*). CISs are macromolecular injection devices with homologies to the contractile tails of phages, comprising a contractile sheath-tube module that is assembled on a baseplate structure. Upon firing, contraction of the sheath expels the inner tube and propels it into a target cell. CISs are classified into two major groups according to their mode of action: extracellular CISs (eCISs) and type VI secretion systems (T6SSs). eCISs are released into the medium and bind to a target cell, followed by firing and translocation of cargo (*18*, *19*, *22*, *23*). T6SSs are anchored to the inner membrane through their baseplate and accessory components, and they can fire into neighboring cells in a cell-cell contact-dependent fashion (*17*, *24*, *25*). Although rhapidosomes have similarities to CISs, their role and mode of action in ixotrophy are unclear.

In this study, we set out to explore the molecular mechanism of ixotrophy to answer the following questions: (i) How is the prey caught? (ii) How is the prey killed? (iii) How is ixotrophy regulated? (iv) Why do cells use ixotrophy?

Results

We studied ixotrophy in the strain *Aureispira* sp. CCB-QB1 (*26*) (hereafter referred to as "*Aureispira*" or "attacker") and established it as a model organism. Fluorescent light microscopy (LM) showed that filaments of *Aureispira* typically comprised ~5 to 10 individual cells (fig. S1A). Previous studies showed an ixotrophic behavior of *Aureispira* against *Vibrio* species on solid and in liquid medium (*9*, *27*). To first understand the dynamics on solid surfaces at a single-cell level, we performed time-lapse LM imaging of *Aureispira* cells co-incubated with *Vibrio campbellii* as prey on an agarose pad. *Aureispira* filaments revealed rapid gliding motility (up to ~2 μm/s), resembling the typical SprB-mediated crawling movement described for other filamentous *Bacteroidetes* (*28*). *Aureispira* filaments were frequently seen to use this gliding motility to either bulge out to approach a *V. campbellii* cell (Fig. 1A and movie S1) or to glide "head-on" toward a *V. campbellii* cell (fig. S1B and movie S2). In ~78% of such cell-cell contacts (n = 130), the *V. campbellii* cells subsequently showed signs of cell lysis (Fig. 1B). Among them, many *V. campbellii* cells (~60%) immediately lysed within seconds after the cell-cell contact, whereas in ~18% of the cell-cell contacts, the *V. campbellii* cells showed signs of rounding and often lysed at a later stage (Fig. 1B and fig. S1C). Such antagonistic effects were not seen in the absence of cell-cell contact (n = 102). The need for contact was further supported by a bulk killing assay on a solid medium, in which killing of *V. campbellii* was only observed by coincubation of *V. campbellii* with live *Aureispira* cells, not with culture supernatant or heat-inactivated attacker cells (Fig. 1C and fig. S1D). Even though killing appears to be contact-dependent, ixotrophy also functions in a liquid medium. We hypothesized that *Aureispira* must be able to make contact with prey cells efficiently. To visualize this behavior, we mixed *Aureispira* with *V. campbellii* in liquid medium and found that, in fact, *Aureispira* was decorated by multiple *V. campbellii* cells within only a few seconds from the onset of coincubation, which is consistent with previous reports (*8*) (Fig. 1D and movie S3). Notably, the specificity toward a certain prey occurs only in liquid medium, and a wider range of prey was killed indiscriminately on solid agar surface (fig. S1E). We conclude that ixotrophy-mediated killing functions in liquid and on solid media and requires direct cell-cell contact.

Cell envelope–associated supramolecular machines

To observe ultrastructures that may be involved in catching and killing of the prey, we plunge froze *Aureispira* cells on electron microscopy (EM) grids and imaged them by cryo–electron tomography (cryo-ET). Individual cells within a filament were separated by a septum and had a typical Gram-negative cell envelope that was associated with distinct supramolecular machines (Fig. 1, E and F; fig. S1F; and movie S4). Attached to the outer membrane (OM) were numerous rigid rods with terminal "grappling hook"–like structures (hereafter

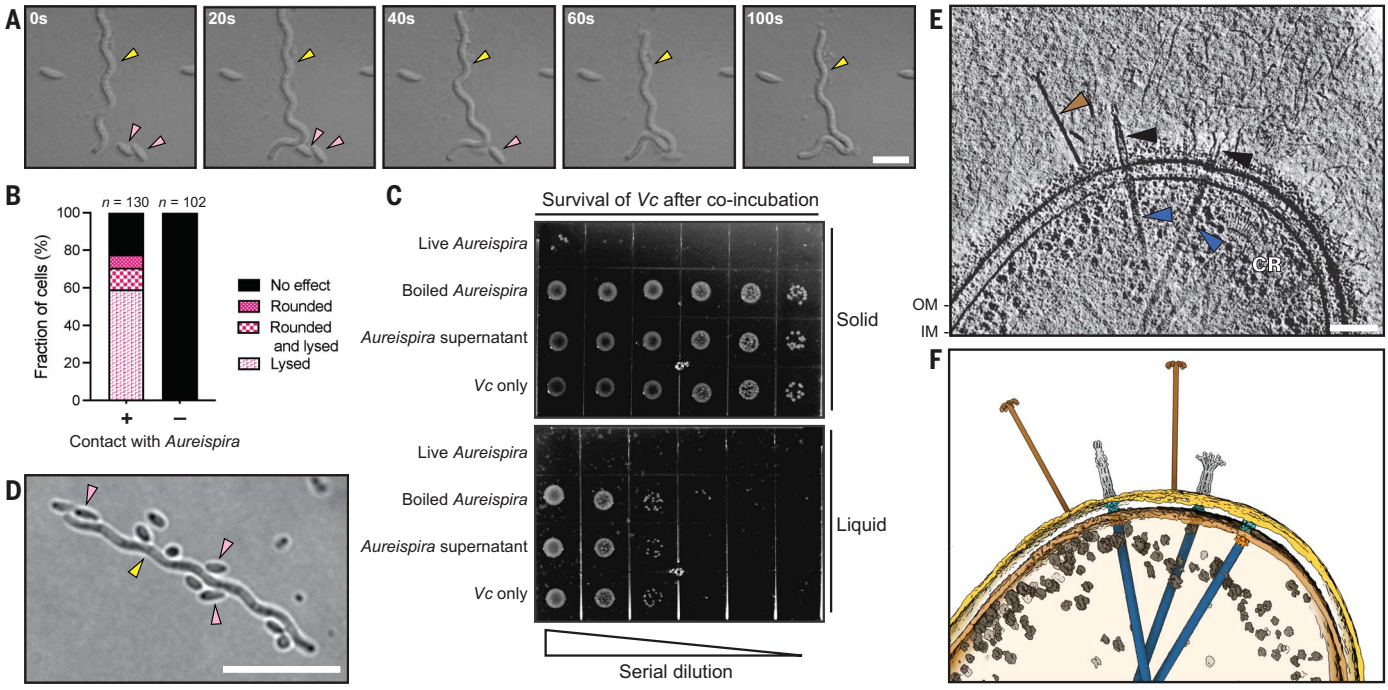

Fig. 1. *Aureispira* shows contact-dependent killing in liquid and on solid media and expresses an arsenal of supramolecular machines. (**A**) Time-lapse light microscopy (LM) images show an *Aureispira* filament (yellow arrowhead) approaching *V. campbellii* prey cells (pink arrowheads) followed by rapid lysis of the prey. Scale bar, 5 μm. (**B**) Quantification of the fate of *V. campbellii* prey cells in time-lapse LM movies revealed that ~80% of *V. campbellii* cells showed signs of cell lysis after cell-cell contact with *Aureispira*. No signs of cell lysis (e.g., cell rounding, cell disappearance) were observed for *V. campbellii* cells without direct contact with *Aureispira* filaments. Sample size *n* is indicated at the top of the graph. (**C**) Serial dilution of prey cells after coincubation killing assays suggests that ixotrophy killing is contact-dependent. *V. campbellii* (*Vc*) was coincubated either in liquid culture (bottom panel, 6 hours of coincubation) or on a solid agar plate (top panel, 24 hours of coincubation) with differently treated *Aureispira* cells (indicated on the left). The cultures were serially diluted and dropped onto an agar plate to visualize the survival of *V. campbellii*. See fig. S1D for the quantification of *V. campbellii* before the start of the coincubation assay. (**D**) LM image shows an *Aureispira* filament (yellow arrowhead) decorated with *V. campbellii* cells (pink arrowheads) after coincubation in liquid culture. Scale bar, 10 μm. (**E**) Slice through a cryo-tomogram of *Aureispira* reveals several supramolecular machineries (slice thickness: 13.8 nm). Attached to the OM were grappling hook–like structures and multiple IM-bound T6SS-like apparatuses. T6SSs were often associated with extracellular antenna-like densities that were seen in two distinct conformations. CR, chemoreceptor arrays. Scale bar, 100 nm. (**F**) A segmentation of the tomogram in (E). OM, yellow; IM, light brown; grappling hooks, brown; T6SS sheaths, blue; T6SS baseplates, orange; T6SS transenvelope complexes, turquoise; antennae, light gray; ribosomes, dark gray.

referred to as "grappling hooks"). Furthermore, all cells exhibited multiple T6SS-like apparatuses in mostly extended and rarely contracted conformations. T6SSs were often associated with extracellular "antenna"-like structures. Some cells also showed putative chemoreceptor arrays (CR) in the cytoplasm (fig. S1G).

Interaction of grappling hooks with prey flagella

To test whether the grappling hooks contact *V. campbellii* cells in liquid medium, we imaged a mixture of attacker and prey cells. Given the thickness of the sample, the frozen cells had to be thinned by cryo–focused ion beam (cryo-FIB) milling before cryo-ET imaging (*29*–*31*). Our cryo-tomograms revealed that grappling hooks interacted with the flagella of the prey cells (Fig. 2A), which were identified by their characteristic ultrastructural features (fig. S2A). To test the relevance of this interaction for ixotrophy in liquid and on solid medium, we coincubated *Aureispira* with *V. campbellii* wild-type (WT), *V. campbellii* flagellin deletion mutants (Δ*flagellin*, lacking flagella), and *V. campbellii* revertant (fig. S2, B and C), respectively. LM imaging immediately after mixing in liquid medium revealed that prey cell decoration of *Aureispira* was drastically reduced for a *V. campbellii* Δ*flagellin* mutant, in contrast to a revertant of the mutant that showed WT-like decoration of *Aureispira* (Fig. 2B; fig. S2, D to G; and movies S3, S5, and S6). Finally, a killing assay with either *V. campbellii* WT, *V. campbellii* Δ*flagellin*, or *V. campbellii* revertant indicated slower killing rates for the Δ*flagellin* mutant in liquid (Fig. 2C and table S1) but no difference when coincubated on solid agar (fig. S2H). These results suggest that, in liquid culture, cell-cell contacts between *Aureispira* and *V. campbellii* are facilitated by the interaction of *Aureispira* grappling hooks with *V. campbellii* flagella.

Structure of grappling hooks—a heptameric type IX secretion system substrate

We set out to identify and structurally characterize the grappling hook. Multiple grappling hooks with a uniform length (240 ± 4 nm; mean ± SD; $n = 55$) were distributed along the cell body in every cryo-tomogram ($n = 146$) (Fig. 2D). Subtomogram averaging of the distal end revealed a terminal structure consisting of seven hooklike densities (Fig. 2E and fig. S3). For protein identification, grappling hooks were sheared off, further purified, and subjected to single-particle cryo–electron microscopy (cryo-EM) (fig. S4 to S6). We determined eight distinct density maps at a global resolution between 3.4 and 3.8 Å that correspond to different regions along the grappling hook stem module (shown in different colors in Fig. 2E; local resolution of density maps is shown in fig. S7). Consistent with the presence of seven terminal hooks, the structures of all stem regions show a C7-symmetry with a hollow lumen. For identification of involved proteins, the program ModelAngelo (*32*) was used to predict the primary amino acid sequence on the basis of the density maps. These sequences were then blasted against the *Aureispira* genome. The eight density maps all correspond to the same protein [WP_231512793.1/WP_156039871

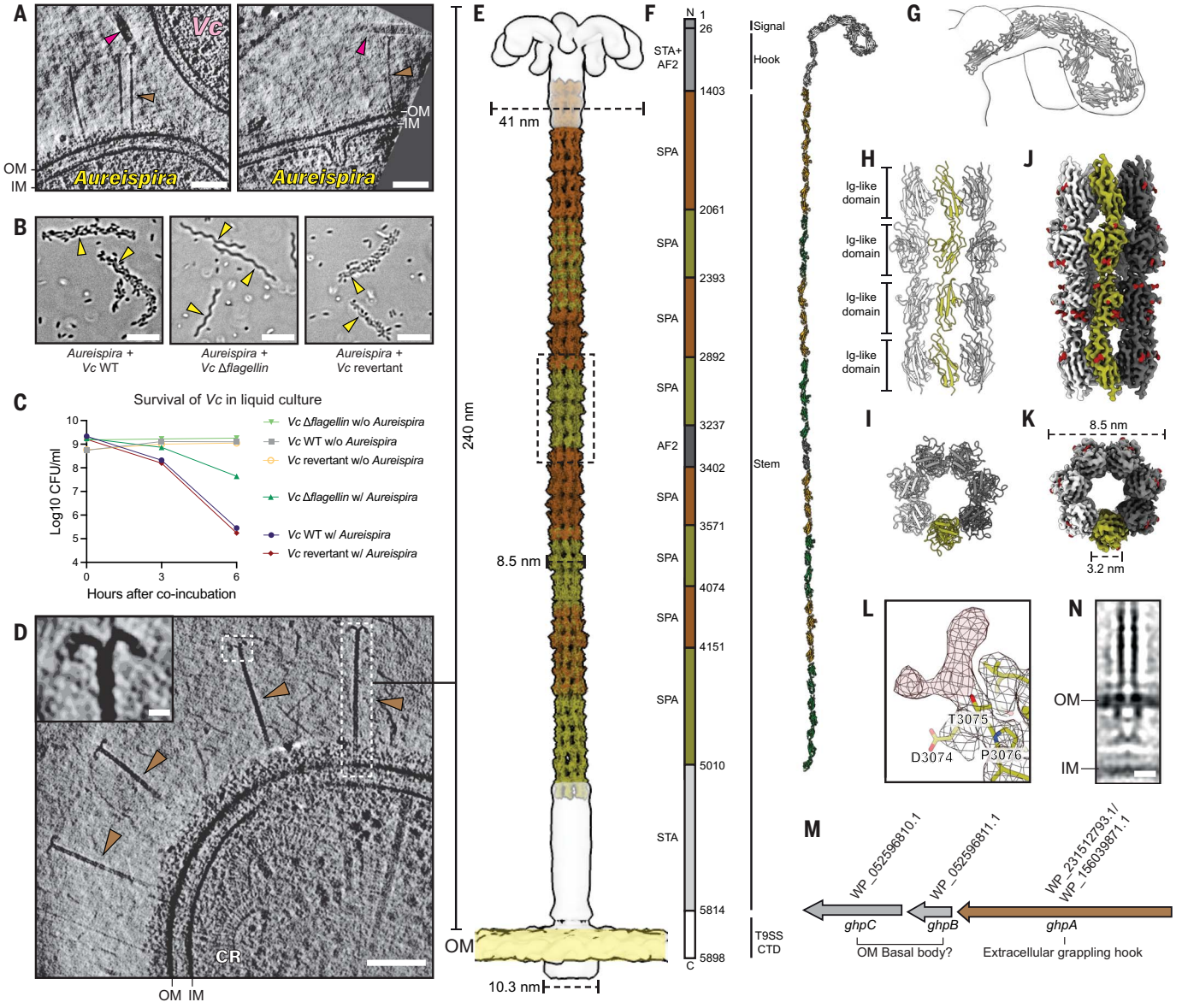

Fig. 2. Heptameric grappling hooks interact with prey flagella. (**A**) Cryo-ET of cryo-FIB–thinned *Aureispira*–*V. campbellii* prey mixture reveals interactions between *Aureispira* grappling hooks (brown arrowhead) and prey flagella (magenta arrowhead). Shown are 13.8-nm-thick slices. Scale bars, 100 nm. (**B**) LM imaging of *Aureispira* coincubated in liquid culture with the same amount of either *V. campbellii* WT (left; image taken 40 s after mixing), *V. campbellii* flagella mutant (Δ*flagellin*, middle; image taken 144 s after mixing), or *V. campbellii* revertant (right; image taken 155 s after mixing). Only flagellated prey cells were efficiently caught on the *Aureispira* cell surface. Yellow arrowhead, *Aureispira* filaments. Scale bars, 10 μm. (**C**) Survival of *V. campbellii* strains after coincubation with *Aureispira* in shaking liquid culture reveals a reduced killing ability of *Aureispira* against *V. campbellii* Δ*flagellin*. Colony forming units (CFU) of three biological replicates were quantified at the time points indicated with three technical repeats each. As control, *V. campbellii* WT and mutant cultures were quantified simultaneously without the addition of *Aureispira*. (**D**) A slice through a cryo–electron tomogram showing an *Aureispira* cell with several homogeneous extracellular grappling hooks (brown arrowhead). Scale bar, 100 nm. Shown is 13.8-nm-thick slice. Magnified view of the distal end of a grappling hook is provided in the inset. Scale bar, 10 nm. (**E**) A composite density map combining results of subtomogram averaging and single-particle cryo-EM to show the overall structure of a grappling hook. Density maps obtained by subtomogram averaging are shown in light gray, and density maps obtained from single-particle cryo-EM are shown in brown or green. OM, yellow. (**F**) GhpA schematic representation (left), indication of structural modules (middle), and composite atomic model (right). Methodologies used to determine the structure of GhpA fragments and their corresponding amino acid residues are indicated next to the schematic. AF2, AlphaFold2 prediction; STA, subtomogram averaging; SPA, single-particle cryo-EM. (**G**) Atomic model of the distal hook was predicted by AlphaFold2 (residues 26 to 1402, gray) and fitted into the subtomogram averaging density map. (**H** and **I**) Atomic model [side view in (H), top view in (I)] of the stem region of GhpA [residues 2892 to 3236, corresponding to the dashed box in (E)], revealing seven parallel strands of GhpA with a hollow lumen and individual strands composed of successive Ig-like domains. See fig. S9 for atomic models of other fragments. Individual GhpA strands are shown in different shades of gray and green. (**J** and **K**) Surface rendering of the SPA density map of the fragment of the grappling hook stem region [side view in (J), top view in (K); corresponding to dashed box in (E)]. Bulky densities, which could not be assigned to an amino acid side chain, are shown in red and likely correspond to glycosylation sites. See fig. S9 for surface renderings of SPA density maps of other fragments. Color code as in (H) and (I). (**L**) An example showing the SPA density map of a potential branched glycan on the grappling hook stem at Thr^{3075}. The potential glycan is highlighted in light red. (**M**) Schematic of the grappling hook gene cluster. Next to GhpA, it encodes putative OM basal body proteins GhpB (homolog of PorP) and GhpC (homolog of PorE). (**N**) Longitudinal slice through C7 rotationally symmetrized subtomogram average of the OM basal body of grappling hooks. Scale bar, 10 nm.

(spread across two contigs)], which we will refer to as grappling hook protein A (GhpA). Seven protomers of GhpA align longitudinally to form the grappling hook emanating from the OM.

GhpA is a 5898 amino acid residue–long protein with a predicted molecular weight of 610 kDa (Fig. 2F). Sequence and structure homology analyses revealed an N-terminal Sec secretion system signal peptide (residues 1 to 25), followed by a bacterial adhesin–like domain that corresponds to the distal hook module. The hook module could not be resolved by single-particle cryo-EM owing to its flexibility. An AlphaFold2 prediction of the N-terminal region (residues 26 to 1402), however, resulted in a loop-like structure, which fits with high confidence into the subtomogram average (Fig. 2G).

The stem module is composed of seven longitudinally aligned GhpA strands, which form a straight and hollow structure (Fig. 2, F, H, and I). The GhpA stem region comprises 52 slightly varying immunoglobulin (Ig)–like repeats. Lateral interactions between the protomers are mediated by intermolecular hydrogen bonds (fig. S8, A and B). Furthermore, a multitude of intramolecular disulfide bonds and hydrogen bonds were found between nearby Ig-like domains (fig. S8). Together, these interactions are likely the basis for the straight and rigid architecture of the stem. In addition, the surface of the stem module shows bulky densities nearby threonine and serine residues that likely correspond to O-glycosylation sites (Fig. 2, J and K, and fig. S9). These potential glycans are found in all the Ig-like domains, and they are often branched (Fig. 2L and fig. S9), consistent with the general glycosylation pattern found in other *Bacteroidota* species (*33*, *34*). The proximal region of the stem was less well resolved, presumably because the grappling hooks were sheared off during purification, inducing structural flexibility in this region.

The GhpA C terminus encodes a type IX secretion system (T9SS) substrate sorting domain, and we found the core genes of the T9SS machinery in the *Aureispira* genome (table S2). In *Porphyromonas gingivalis*, a T9SS substrate is speculated to be anchored on the cell surface by interacting with PorP and PorE (*35*), which encode OM beta-barrel and OmpA-like peptidoglycan binding domains, respectively. We also detected such homologs downstream from *ghpA* (here referred to as *ghpB* and *ghpC*) (Fig. 2M and fig. S10). Subtomogram averaging of the anchoring region of grappling hooks revealed a structure located in the OM and periplasm (Fig. 2N). Altogether, we conclude that grappling hooks are assembled from a heptameric T9SS substrate.

A T6SS with distinctive features

Next, we set out to investigate the structure and the role of *Aureispira* T6SSs (Fig. 1, E and F). We first identified a candidate T6SS gene cluster (Fig. 3A) in the *Aureispira* genome (*26*). The cluster comprises genes for typical structural components, which we renamed *cis1* to *cis16* according to previously characterized CISs (*19*, *21*, *22*) (table S3). Proteomics of a crude purification confirmed that *Aureispira* T6SSs were encoded by these genes (Fig. 3A, fig. S11A, and table S4). Close relatives of the *Aureispira* system are the eCIS in *Algoriphagus machipongonensis* (*22*), the eCIS in *Pseudoalteromonas luteoviolacea* (*18*), the thylakoid-anchored CISs in cyanobacteria (*21*), and the T6SS^{iv} in *Ca.* A. asiaticus (*20*) (fig. S12). On the basis of these phylogenetics and cryo-ET imaging, we classify the *Aureispira* T6SS as subtype *iv* (T6SS^{iv}). The previously reported rhapidosomes (*15*) are likely T6SS^{iv} structures.

In cryo-tomograms, extended T6SSs were always seen anchored to the inner membrane (IM) (Fig. 3, B and C). Extended T6SSs had a homogeneous length of 420 ± 8 nm (mean ± SD; n = 45), consistent with the presence of a putative tape measure protein (Fig. 3A, *cis14*). On average, we detected 4.6 extended T6SSs per tomogram (fig. S11B). Notably, *Aureispira* T6SSs were often associated with extracellular antenna–like structures. These antennae showed two distinct conformations, which we term "closed" (58%; 278 out of 482) and "open" (26%; 124 out of 482) (Fig. 3, B and C, and fig. S11C).

We then performed subtomogram averaging of the individual T6SS modules—antenna, transenvelope complex, baseplate, and sheath. The antenna in the closed conformation revealed a complex C6-symmetric architecture, a length of 132 nm, and a width of 10 to 19 nm (Fig. 3, D to F, and figs. S13, A to C, and S14, A, C to E, and I). The open conformation was much shorter (82 nm) and featured a similar architecture at the base (figs. S3F and S14, B, F to H, and I). The distal part of the open conformation showed a substantial widening (width of 62 nm) of the six arms that each split into two further protruding densities (Fig. 3F and fig. S14, F and J). To our knowledge, except for the much simpler extracellular structures connected to a T6SS in *Myxococcus* (*36*), such elaborate extracellular T6SS-associated structures have not been reported.

The C6-symmetric transenvelope complex consisted of three main parts (Fig. 3, D, E, G, and H, and figs. S13, A, D, and E, and S15, A to K). Two components were associated with the OM and IM, respectively. A third periplasmic part complements the structure, resulting in a continuous OM-IM spanning complex. This transenvelope complex is fundamentally different from the C5-symmetric transenvelope complex from the canonical T6SS^{i} (*25*). Accordingly, we did not detect homologs of the responsible genes from T6SS^{i} (*tssJLM*) and T6SS^{iii} (*tssNOPQR*) (*37*) in the *Aureispira* genome. The structure also presents a major variation compared with the T6SS^{iv} in *Ca.* A. asiaticus, which lacks a transenvelope complex altogether (*20*).

The T6SS baseplate is also C6-symmetric, and its architecture is generally consistent with high-resolution structures of thylakoid-anchored CISs from cyanobacteria (*21*) and eCISs from *Algoriphagus* (*22*) (Fig. 3, D, E, I, and J, and figs. S13, A, F, and G, and S15, L to R). All of these systems feature an extension of Cis11, which was shown to form a cage-like structure around the spike. This extension is conserved in the *Aureispira* Cis11, and a similar cage structure around the spike is seen in the baseplate average (Fig. 3K). The comparison with the T6SS^{iv} in *Ca.* A. asiaticus (*20*) reveals that, in both systems, contact to the IM seems to be mediated by a set of six anchoring densities as well as by the cage (Fig. 3, D, E, and I).

Killing of prey by T6SS

Next, we set out to understand whether the novel T6SS was involved in ixotrophy killing. Physical puncturing by the T6SS inner tube has long been hypothesized but never visualized (*38*–*40*). Thus, we coincubated *Aureispira* and *V. campbellii* for 2 to 8 min and performed cryo-FIB milling and cryo-ET. We captured three attacker-prey contacts, showing a contracted sheath and its expelled inner tube protruding from the attacker and puncturing the OM of the prey (Fig. 3, L and M, and movie S7). In one example, the OM showed signs of vesiculation and disruption at the puncturing site. The detection of three puncturing events in only 86 cryo-tomograms of ~150- to 200-nm-thick lamellae indicates that these events are relatively long-lived or very frequent.

Having established that the T6SS has a disruptive effect on the prey cell envelope, we further investigated whether it was also responsible for killing. Our attempts to establish a genetic system by site-directed mutagenesis were unsuccessful, given the multicellularity of the strains and the absence of genetic tools for close relatives. In the process, however, we identified several *Aureispira* derivatives (T6SS-negative) from which we could not purify T6SS sheath and which did not show any assembled T6SSs in cryo-tomograms (fig. S16, A to C, and table S4). Genome sequencing of the WT and T6SS-negative derivatives revealed that each mutant strain had an insertion of an "insertion sequence" (IS) into T6SS genes (Fig. 3N and fig. S16, D to G). All three ISs were different, and we therefore named them IS*Aursp1* (for IS *Aureispira* sp. 1), IS*Aursp2*, and IS*Aursp3*. ISs are the simplest mobile genetic elements that encode only a transposase gene that can insert into various sites in the genome (*41*). Whereas IS*Aursp1* and IS*Aursp2* were inserted into different positions

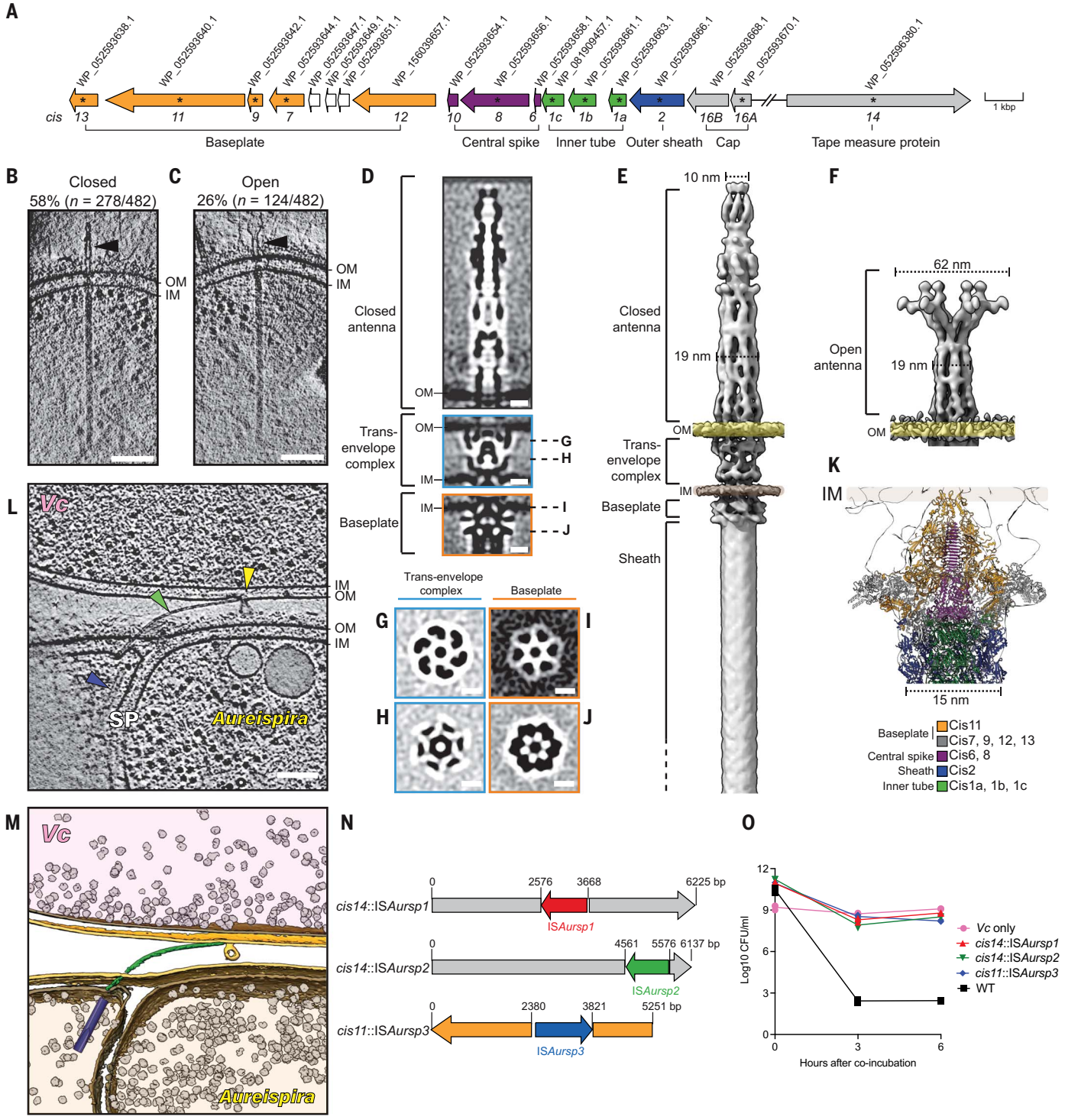

Fig. 3. A type VI secretion system with distinctive features kills prey. (**A**) Schematic representation of the *Aureispira* T6SS^{iv} gene cluster. Accession numbers are indicated above, and genes were renamed *cis1* to *cis16*. The assignment of genes to functional modules is indicated along the bottom. Asterisks indicate components that were detected in purification by mass spectrometry. (**B** and **C**) Examples of cryo-tomograms of *Aureispira* T6SSs with extracellular antennae (black arrowheads) in either "closed" (B) or "open" conformations (C). Quantification of observed antenna conformation is indicated along the top. Scale bars, 100 nm. Thickness of the cryo-ET slices: 13.8 nm. (**D**) Slices through subtomogram averages of extracellular antenna, trans-envelope complex, and baseplate of *Aureispira* T6SSs, respectively. Scale bars, 10 nm. (**E**) Composite isosurface representation of the subtomogram averages of closed antenna, transenvelope complex, baseplate, and sheath-tube modules. (**F**) Isosurface representation of the subtomogram average of the open antenna. (**G** to **J**) Perpendicular slices through the C6-symmetrized subtomogram average of the transenvelope complex [(G) and (H)] and the baseplate [(I) and (J)]. The positions of the slices are indicated in (D). Scale bars, 10 nm. (**K**) Docking of the atomic model of thylakoid-anchored CIS (PDB ID 7B5H) into the density map of the subtomogram average of the *Aureispira* T6SS baseplate reveals conserved elements such as a cage (Cis11, orange)

surrounding the spike (Cis8, purple). (**L**) Slice through a cryo-tomogram of a cryo-FIB–thinned *Aureispira*–*V. campbellii* mixture reveals a contracted T6SS sheath (blue arrowhead) and an associated expelled inner tube (green arrowhead). The inner tube is seen penetrating the OM of *V. campbellii* (yellow arrowhead), apparently resulting in membrane vesiculation. SP, septum. Thickness of the slice: 13.8 nm. Scale bar, 100 nm. (**M**) Segmentation of the tomogram shown in (L). OM, yellow; IM, light brown; contracted T6SS sheath, blue; T6SS inner tube, green; ribosomes, gray. (**N**) Schematic illustrating the interruption of T6SS genes by insertion sequences (ISs) in T6SS-negative *Aureispira* derivatives. (**O**) Quantification of CFU of prey cells during killing assay (in liquid culture) with *Aureispira* WT or *Aureispira* T6SS-negative derivatives. CFU of *V. campbellii* were quantified at several time points by serial dilution of the culture and plating on agar, revealing that T6SS-negative *Aureispira* derivates were unable to kill *V. campbellii*.

of gene *cis14* (tape measure protein, strains *cis14*::IS*Aursp1* and *cis14*::IS*Aursp2*), IS*Aursp3* was inserted into gene *cis11* (baseplate component, strain *cis11*::IS*Aursp3*). As all three ISs are present elsewhere in the genomes of WT with an additional copy in each mutant strain, the origins of the T6SS-disrupting ISs were likely duplication events (table S5).

Finally, we performed killing assays with WT and T6SS mutant strains and observed that the ability to kill was completely abolished in the T6SS-negative strains (Fig. 3O). Time-lapse imaging showed that the mutants were still able to glide and made repeated contact with prey cells on a solid surface (movie S8). Furthermore, they captured prey cells onto their surface in liquid culture (fig. S16H and movie S9), however, lysis of prey cells was never observed. In summary, *Aureispira* expresses abundant T6SSs with distinctive structural features that are required for killing, and the system can be deactivated by endogenous ISs.

Nutrient availability toggles activity of T6SS by insertion sequences

The spontaneous inactivation of the T6SS was observed in full medium, which posed the question of whether the T6SS activity was affected by nutrient availability. We therefore set out to investigate whether inactivation was reversible upon starvation. First, we determined the transcription levels of two genes involved specifically in IS excision. The IS-excision enhancer *iee* is an error-prone DNA polymerase previously found to enhance the IS excision rate (*42*, *43*), whereas *recB*, a factor of the DNA double-strand break repair machinery, is required for successful IS excision (*44*, *45*). We compared transcription levels of *iee* and *recB* in cells that were cultured in full medium versus minimal medium and found that transcription of both genes was significantly up-regulated during starvation (Fig. 4A and fig. S17A).

We therefore hypothesized that under nutrient-limiting conditions, T6SS-negative strains may reactivate T6SS by IS excision. To test this, we cultured a T6SS-positive (WT) and a T6SS-negative (*cis14*::IS*Aursp2*) strain under nutrient-limiting conditions but in the presence of *V. campbellii* (Fig. 4B). The optical cell density (OD_{600}) was measured daily and served as a general indicator for *V. campbellii* survival. As expected, the T6SS-positive WT efficiently killed *V. campbellii*, resulting in very low OD_{600} values (Fig. 4C). In contrast, in three independent cultures of the T6SS-negative mutant *cis14*::IS*Aursp2*, the OD_{600} values remained high over the course of ~30 days, indicating the absence of killing activity. On days 33 and 36, respectively, the OD_{600} values in two of the mutant cultures suddenly dropped, indicating the reactivation of killing. Indeed, the excision of IS*Aursp2* in *cis14* was confirmed by polymerase chain reaction (PCR) and sequencing (Fig. 4, D and E, and fig. S17B). Both excision events resulted in the deletion of three and six base pairs, respectively, compared with WT (Fig. 4E). We conclude that IS elements constitute a mechanism providing genetic variants for selection by deactivating expression of dispensable genes in nutrient-rich conditions by duplication events and by reactivating them in nutrient-limiting conditions by excision events.

Nutrient uptake from killed prey cells

Next, we turned to the question of why *Aureispira* kills prey cells. To test whether *Aureispira* takes up nutrients from prey cells upon killing, *V. campbellii* was labeled with deuterium (D). We first confirmed that D-labeled *V. campbellii* can still be killed by *Aureispira* (fig. S18A). The D-labeled prey cells were then coincubated for 1 hour with unlabeled *Aureispira* cells. We then measured the D-labeling status of the *Aureispira* cells using single-cell Raman microspectroscopy (Fig. 5A). For each *Aureispira* filament, we quantified the D-labeling status by normalizing the signal intensity of the carbon-deuterium (C-D) peak with that of the carbon-hydrogen (C-H) peak (a proxy for cell biomass) (*46*). The D-labeling status of T6SS-positive *Aureispira* was significantly higher compared with the T6SS-negative strain (Fig. 5B and fig. S18, B and C). These results suggest that *Aureispira* takes up and likely metabolizes nutrients from killed *V. campbellii*.

Ixotrophic predator abundance correlates with Vibrionaceae populations

Finally, we asked whether the analysis of an environmental dataset would support the hypothesis that ixotrophy was an important predatory activity in the wild. Because *Vibrionaceae* are common prey for ixotrophic predators (*8*, *9*, *27*), we analyzed the Nahant time series, which consists of daily water samples from a coastal region over a 93-day period (*47*), for correlated occurrences. We first identified 35 pairs of *Vibrionaceae* and *Saprospiraceae* amplicon sequence variants, whose abundance significantly correlated to each other over the entire time series with a characteristic time lag indicating coupled dynamics (data S1). This behavior is consistent with a predator-prey relationship. Because amplicon sequences typically encompass relatively broad phylogenetic groups, we focused in a second analysis on the dynamics of one very large *Vibrionaceae* bloom from Julian day 238 to 242 (*47*) using deeply sequenced metagenomes to test the specificity of the response from ixotrophic predators. This analysis confirmed that the relative abundance of ixotrophy-positive strains (*Saprospira*) increases after the *Vibrionaceae* bloom. In contrast, the abundance of *A. machipongonensis*, which is an ixotrophy-negative *Bacteroidota* strain (*22*, *48*), does not respond (fig. S19). Overall, these analyses are suggestive that ixotrophy might be an overlooked important predatory lifestyle in this environment.

Discussion

Our proposed model for bacterial ixotrophy involves different functional modules (Fig. 6), depending on the environment. On solid surfaces, T9SS and SprB–mediated motility allows the predator to glide toward prey cells to establish cell-cell contact. In liquid medium, grappling hooks formed by the T9SS substrate GhpA interact with the prey flagella to immobilize the prey on the predators' surface. This is followed by the use of short-range contact-dependent T6SS for killing. Motility has recently been shown to increase the use of short-range weapons (*49*); in an aquatic environment, such a system is likely advantageous over the secretion of a toxin or an eCIS into the medium.

Ixotrophy-like behavior has been reported in filamentous multicellular bacterial species of the *Saprospiria* and *Cytophagia* classes from the phylum *Bacteroidota* (*8*–*13*). Our analysis of available genomes of ixotrophy-positive bacteria revealed the presence and coexistence of gene clusters encoding T6SSs, T9SSs, SprB, and grappling hook protein GhpA in these organisms (table S6). This indicates a conserved molecular mechanism for ixotrophy and its role in mediating access to nutrients in heterogeneous aquatic environments. In fact,

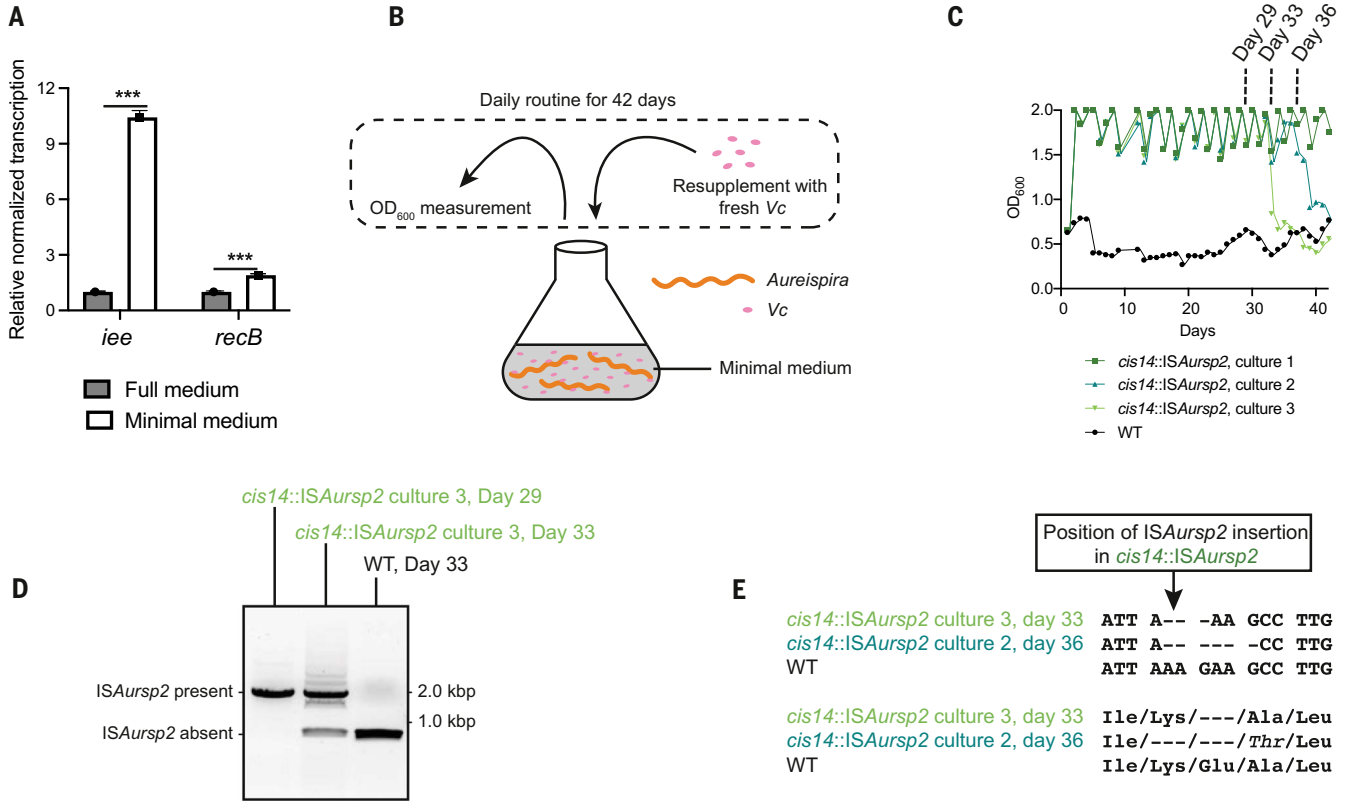

Fig. 4. Insertion sequences control T6SS activity. (**A**) Genes involved in IS excision (*iee* and *recB*) were up-regulated during starvation. Total RNA from *Aureispira* cultured in full or minimal medium was extracted, and *iee* and *recB* transcripts were quantified. The transcription level was normalized using the housekeeping gene *gyrB*. (**B**) Schematic showing the experimental setup that was used to analyze IS excision during starvation. OD_{600} values of the cultures were measured every day and afterward readjusted to OD_{600} = 2 by adding prey cells. Experimental data are shown in (C). (**C**) OD_{600} measurements of the *Aureispira*–*V. campbellii* starvation experiment described in (B). Until day 32, only the WT culture showed killing activity (low OD_{600} values), whereas cultures 1 through 3 (T6SS-negative derivatives) did not kill (as evidenced by high OD_{600} values). On days 33 and 36, respectively, OD_{600} values of cultures 2 and 3 dropped, indicating reactivation of T6SS killing activity. (**D**) IS*Aursp2* excision was confirmed by PCR amplification of a *cis14* fragment (primers shown in fig. S16D). At day 29, IS*Aursp2* was homogenously present in *cis14* of *Aureispira* culture 3. On day 33, we detected a mixture of *cis14* fragments with inserted IS*Aursp2* as well as *cis14* WT fragments. (**E**) PCR products from (D) and fig. S17B were sequenced, revealing that IS excision generated 3- or 6-bp deletions in *cis14*. Sequencing results are shown at the top, and the corresponding translated amino acid sequence is shown at the bottom.

ixotrophy-positive organisms show a broad distribution across diverse sites (table S7). The correlation between abundances of ixotrophic predators and *Vibrionaceae* in an environmental dataset (fig. S19 and data S1) indicates that ixotrophy may play a previously unrecognized role in shaping the marine microbiome.

Our data reveal grappling hooks as an elegant solution to the challenge of establishing efficient cell-cell interactions in a liquid medium. Notably, grappling hook–like surface-anchored cell appendages were previously found in archaea (*50*–*52*). These are known as "hami" and are believed to be involved in the formation of networks consisting of multiple sister cells. Furthermore, recent studies have characterized the role of other extracellular adhesins used by the antagonistic bacteria *Bdellovibrio* and *Vibrio cholerae* to establish cell-cell contact with their prey (*53*, *54*).

In bioinformatic searches, we detected a high abundance of close relatives to the grappling hook protein GhpA in other related *Bacteroidota* species (table S6). Cryo-ET imaging of one representative, *Microscilla marina*, confirmed the presence of grappling hook–like structures (fig. S20A), and structure prediction confirmed the characteristic hooklike architecture at the N terminus (fig. S20B). This result indicates broad conservation of the grappling hook structure and its function across ixotrophy-positive bacteria. The formation of a heptameric palm tree–like module at the N-terminal distal end may be needed to expose multiple binding sites for the target. This N terminus shows similarities to adhesins from the antigen I/II family of streptococci [Protein Data Bank (PDB) IDs 3QE5, 4TSH, and 2WQS]. Many of these adhesins bind Ca^{2+} ions (*55*), consistent with ixotrophy being a Ca^{2+}-dependent phenomenon (*9*).

GhpA has similarities to the protein SprB, the key extracellular factor involved in gliding motility in members of *Bacteroidota* (*28*). While both SprB and GhpA are large proteins (5898 amino acid residues for *Aureispira* GhpA and 6497 for *Flavobacterium johnsoniae* SprB) with Ig-like repeats and a C-terminal T9SS sorting domain, SprB has been proposed to form flexible filamentous extracellular appendages (*56*, *57*). An SprB homolog is also found in the genome of *Aureispira* (WP_052599872.1), which is consistent with gliding motility (Fig. 1A) (*9*) and potentially corresponds to the thinner extracellular filaments observed in cryotomograms of *Aureispira* cells (fig. S21). SprB may not multimerize like GhpA and thus may form thinner and more flexible structures.

For killing prey, we found that ixotrophy requires the functional T6SS subtype *iv*. The *Aureispira* T6SS features a distinctive trans-envelope complex and elaborate extracellular antennae in two different conformations, whose protein compositions remain elusive. We speculate that these adaptations could function in signal transduction from extracellular space

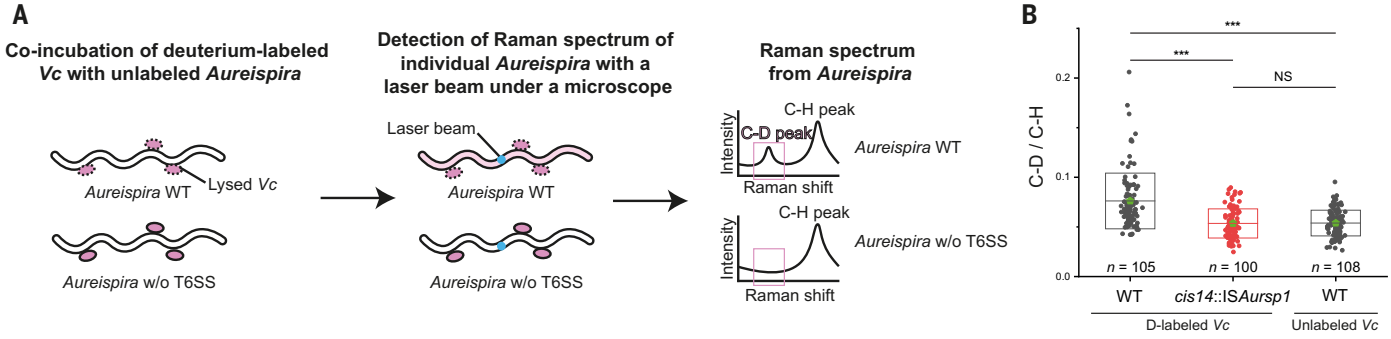

Fig. 5. *Aureispira* takes up substrate from labeled prey. (**A**) Schematic showing the experimental setup of Raman microspectroscopy measurements for testing substrate uptake by *Aureispira* from *V. campbellii* prey cells. The right panel shows illustrative Raman spectra. See fig. S18, B and C, for examples of experimental spectra. (**B**) After coincubation, the deuterium (D) signal can be detected in T6SS-positive (but not in T6SS-negative) *Aureispira* cells using Raman microspectroscopy. The deuterium signal intensity of *cis14*::IS*Aursp1* cells was comparable to that of *Aureispira* WT coincubated with unlabeled *V. campbellii*. The box represents mean (also indicated by the light-green pentagon) ± SD: 0.076 ± 0.028 for WT coincubated with D-labeled *V. campbellii*; 0.054 ± 0.015 for *cis14*::IS*Aursp1* coincubated with D-labeled *V. campbellii*; and 0.054 ± 0.013 for WT coincubated with unlabeled *V. campbellii*. Statistical significance between the samples was assessed using Kruskal-Wallis analysis of variance (ANOVA) followed by post hoc Dunn's multiple comparison test [***$P < 0.001$; NS (not significant), $P > 0.05$].

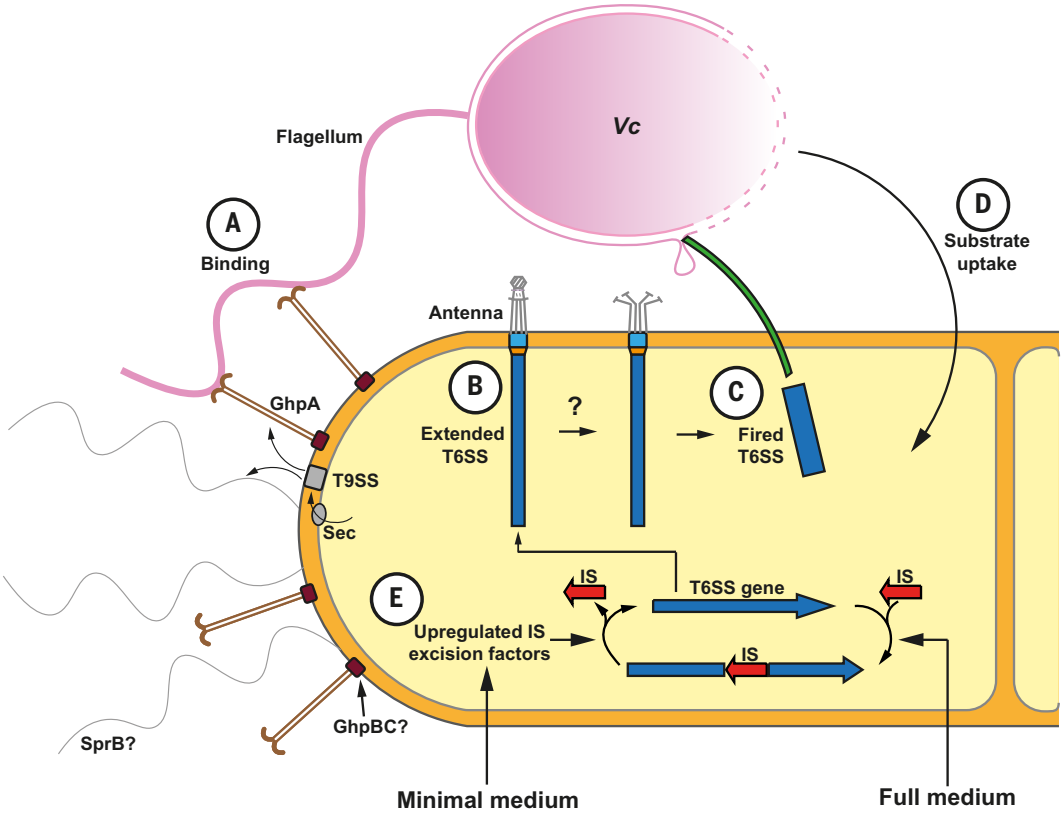

Fig. 6. Integrative model of ixotrophy. (**A**) GhpA is translocated by the Sec/T9SS and assembles into heptameric OM-attached grappling hooks (brown). These grappling hooks mediate the catching of *V. campbellii* flagella in liquid culture. On solid medium, SprB-mediated gliding motility generates cell-cell contacts. (**B**) For the subsequent killing of *V. campbellii*, *Aureispira* expresses multiple T6SS^{iv} (sheath-tube module, blue; baseplate, orange; transenvelope complex, turquoise). T6SS^{iv}-associated extracellular antennae (gray; seen in two distinct conformations) may be involved in signal transduction and triggering of firing. (**C**) T6SS^{iv} firing expels the inner tube and propels it into *V. campbellii*, where it causes cell envelope defects and lysis. (**D**) Released *V. campbellii* components are taken up by *Aureispira*. (**E**) Under nutrient-rich conditions, ixotrophy is switched off by endogenous ISs that integrate into T6SS genes. Upon encountering nutrient-limiting conditions, IS excision factors are up-regulated, and ixotrophy is reactivated by the excision of ISs.

to the T6SS baseplate, thereby triggering firing when a prey cell is in close proximity. This hypothesis is supported by our observation that contracted T6SSs were almost always absent from *Aureispira* cells that were cultured without prey, whereas contracted T6SSs were frequently seen in cells that were coincubated with prey (fig. S22).

Another notable feature of the *Aureispira* T6SS is the stable inner tube. Direct visualization showed the tube inflicting cell envelope defects on the prey cell (Fig. 3, L and M). It remains open whether such potential mechanical stress is complemented by additional effectors. *Aureispira* encodes potential effector candidates that contain DUF4157 domains, which are associated with CIS effectors in other organisms (*22*, *58*, *59*). Our LM observation of prey cells rounding in response to attacker-prey contacts (fig. S1C) is consistent with the action of a peptidoglycan-degrading effector (*60*).

Ixotrophy can be toggled by the insertion or excision of ISs into structural T6SS genes. ISs are used by different pathogens for the regulation of capsule production (*61*) and metabolic pathways (*62*) and for the variation of O1 antigen (*63*). Selection to evolve such a genomic switch in bacteria could originate in the need to deactivate the expression of energy-costly molecular machineries. Recent studies on *Vibrio*, *Pseudomonas*, and *Bacteroides* strains suggest that T6SS activity does have a fitness cost (*64*–*67*). Ultimately, the imperfection of IS excision (Fig. 4E) (*68*) may promote the evolution of the machinery.

Materials and methods

Bacterial culture conditions

Aureispira sp. CCB-QB1, *V. campbellii*, and their derivatives were cultured in artificial seawater medium [ASWM; 2.4% Instant Ocean (Aquarium Systems), 10 mM HEPES, 0.5% peptone, pH 7.6] at 30°C with constant shaking at 200 rpm or on ASWM plates solidified with 1.5% agar. Marine agar and marine broth (Condalab) were used for culturing *V. campbellii*. *Vibrio cholerae* and *Escherichia coli* were grown in Luria-Bertani (LB) broth or on plates solidified with 1.5% agar at 37°C. All strains used in this study are listed in table S8.

Killing assays

Aureispira and prey were cultured overnight in ASWM. In the morning, the cells were concentrated and resuspended in low nutrient ASWM (L-ASWM; 2.4% Instant Ocean, 10 mM HEPES, 0.05% peptone, pH 7.6) to an OD_{600} of 1.0. Cells were starved in L-ASWM for 2 hours. After starvation, *V. campbellii* cultures were mixed in a 1-to-1 ratio with differently treated *Aureispira* cultures. Mixtures were cocultured for 6 hours. This was followed by serial dilutions and plating or spotting onto marine agar plates for quantification.

For assays on solid agar plates, OD_{600} of overnight cultures were concentrated and resuspended in ASWM to an OD_{600} of 1. 5 μl of differently treated *Aureispira* (see above), and *V. campbellii* cultures were mixed in a 1:1 ratio, applied on L-ASWM agar plates, and incubated for 24 hours. After coincubation, cells were scraped from the agar plate with an inoculation loop and resuspended in 200 μl L-ASWM, followed by serial dilution and plating or spotting onto marine agar plates for quantification.

For assays involving *V. campbellii* derivatives, overnight cultures were starved as mentioned above. *Aureispira* and *V. campbellii* were mixed in a 1-to-2 ratio and either dropped onto a L-ASWM agar plate (in total 9 μl) or mixed in L-ASWM. The mixtures were coincubated at 30°C with shaking at 200 rpm for the liquid cultures for the time indicated. After coincubation, the culture was taken out, serial diluted, and plated onto marine agar plates for quantification of CFUs.

Light microscopy imaging

To image the ixotrophy behavior, *Aureispira* and *V. campbellii* were cultured overnight in ASWM, and on the next day concentrated and resuspended in L-ASWM to an OD_{600} of 1.0. Afterward, cells were starved in L-ASWM for 2 hours. Five microliters of *Aureispira* culture and 5 μl of *V. campbellii* culture were mixed on an 0.5% agarose pad made from L-ASWM. The samples were imaged with a 100× oil immersion objective on a Leica Thunder Imager 3D Cell Culture equipped with a Leica DFC9000 GTC CMOS camera (2048 pixels by 2048 pixels, 65 nm by 65 nm pixel size). For the visualization of DNA and cell envelope, cells were stained with 4′,6-diamidino-2-phenylindole (final concentration of 10 μg/ml) and Mitotracker Green (5 μg/ml), respectively, for 30 min at room temperature in the dark. For time-lapse imaging, the samples were imaged either with the Leica Thunder microscope mentioned above or with a Zeiss wide-field microscope equipped with a Hamamatsu ORCA-ER digital camera. Images were recorded every 5 s over a time course of 30 min. For imaging in liquid culture, *Aureispira* and *V. campbellii* derivatives were cultured and starved as mentioned above. One hundred microliters *Aureispira* culture and 100 μl *V. campbellii* culture were mixed in an eight-well μ-slide (Ibidi) and immediately imaged with the microscope using a 40× objective. All images were further analyzed and processed with Fiji (*69*).

Mutagenesis of V. campbellii

To delete the flagellin genes in *V. campbellii*, 800 base pair (bp)–long sequences located upstream and downstream of the *V. campbellii* flagellins were amplified with Q5 2X master mix (New England Biolabs) and ligated into the restriction site XhoI and SphI in pDM4 followed by transformation of the plasmid into *E. coli* SM10 λ pir by electroporation. The plasmid was inserted into the *V. campbellii* genome by conjugation with *E. coli* SM10 λ pir as described previously (*70*). Briefly, overnight-cultured *V. campbellii* and *E. coli* SM10 λ pir harboring pDM4 plasmid were mixed, and 10 μl of the cultures were pipetted onto a marine agar plate and incubated at 30°C overnight. On the following day, *V. campbellii* conjugants were selected with marine agar plates supplemented with 10 μg/ml chloramphenicol and 50 U/ml polymyxin B. A single colony of a *V. campbellii* conjugant was picked and cultured overnight in marine broth and subsequently plated in the morning onto marine agar plates containing 10% sucrose and 50 U/ml polymyxin B to select for the colonies that lost the suicide plasmid. Colonies were screened for the presence of the suicide plasmid and deletion of the gene with PCR. The process was repeated twice to delete all six flagellin genes separated into two loci in the *V. campbellii* genome. The primers used are listed in table S9.

Purification of flagella from V. campbellii

Flagella of *V. campbellii* were purified as described earlier (*71*) with some modifications. Briefly, a 5 ml *V. campbellii* overnight culture in ASWM was pelleted and resuspended in 1 ml of ASWM followed by vigorous vortexing for 2 min to shear off flagella. Intact *V. campbellii* cells were removed by centrifugation at 8000*g* for 10 min at 4 °C, and the supernatant was subjected to ultracentrifugation at 100,000*g* for 1 hour at 4 °C to pellet the flagella. The flagella pellets were resuspended in 100 μl ASWM.

Purification of grappling hooks

Using 200 ml pre-culture, *cis14*::IS*Aursp1* was inoculated in 2 liters of ASWM and incubated overnight. The cells were harvested (7000*g*, room temperature, 20 min), and the cell pellet was resuspended in 48 ml grappling hook shearing buffer (150 mM NaCl, 20 mM HEPES, pH 7.5, 1x cOmplete EDTA-free protease inhibitor tablet). The shearing protocol was adapted from Gaines *et al.* (*72*). Briefly, the vial with the cell suspension was connected to a peristaltic pump and, under gentle magnetic stirring, continuously passed through two needles (0.8 mm by 40 mm, 4°C, 3 hours, and 0.5 mm by 16 mm, 4°C, overnight) at 25 rpm. The sheared suspension was then centrifuged (21,000*g*, 4°C, 20 min) to remove intact cells and debris.

The supernatant was filtered through a 0.45-μm filter (Spritzenfilter Filtropur, Sarstedt AG) and subjected to ultracentrifugation. The filtered supernatant was layered on top of a sucrose cushion [1 ml of 150 mM NaCl, 20 mM HEPES, pH 7.5, 50% (w/v) sucrose] and centrifuged (250,000*g*, 4°C, 3 hours). The bottommost 1.5 ml was collected and centrifuged again

(21,000*g*, 4°C, 20 min). The supernatant was diluted to 48 ml with grappling hook buffer (150 mM NaCl, 20 mM HEPES, pH 7.5). After an additional round of ultracentrifugation (250,000*g*, 4°C, 3 hours), the resulting pellets were soaked in 75 μl grappling hook buffer overnight at 4°C. Afterward, the pellets were resuspended, centrifuged (21,000*g*, 4°C, 20 min), and the supernatant was used for sucrose gradient ultracentrifugation. To this end, 2.5 ml 50% (w/v) and 3 ml 10% (w/v) sucrose gradient buffer (150 mM NaCl, 20 mM HEPES, pH 7.5 with 50% or 10% sucrose, respectively) were layered on top of each other in ultracentrifuge tubes, and a continuous gradient was generated using a gradient maker (Gradient Master, BIOCOMP). The topmost 200 μl of the gradient was discarded, and 300 μl of the grappling hook sample was gently loaded onto the gradient. The sample was then centrifuged (250,000*g*, 4°C, 3 hours) and 11 × 0.5 ml fractions were collected (F1, bottom-F11, top). F5 was found to contain the most grappling hooks, and thus it was diluted to 6 ml with grappling hook buffer and subjected to another round of ultracentrifugation (250,000*g*, 4°C, 3 hours). The pellet was soaked overnight at 4°C in 100 μl grappling hook buffer, resuspended, and stored at 4°C until further use.

Plunge freezing for cryo-ET and single-particle cryo-EM

To image intact *Aureispira* cells by cryo-ET, the OD_{600} of an *Aureispira* overnight culture was adjusted to 1.0 and subcultured in L-ASWM for 2 hours. Three and a half microliters of the culture was applied onto glow-discharged copper EM grids (R2/1, Quantifoil), automatically blotted, and plunged into liquid ethane and propane mixture (*73*) using a Vitrobot Mark IV (Thermo Fisher Scientific) (*74*). Using a Teflon sheet on one side, samples were blotted only from the back for 8 to 10 s.

To image attacker-prey contacts, overnight cultures of *Aureispira* and *V. campbellii* were starved in L-ASWM for 2 hours. Cell cultures were concentrated to an OD_{600} of 5 to 10 by centrifugation (5000*g* for 4 min) and resuspended in L-ASWM. Afterward, concentrated *Aureispira* and *V. campbellii* cultures were either directly mixed on EM grids and plunge frozen within seconds or first incubated at room temperature for 2 to 8 min. For the latter, 4 μl of the cell mixture was applied three times onto glow-discharged copper EM grids (R2/2, Quantifoil), blotted for 6 s from the back, and frozen as described above.

For single-particle cryo-EM of grappling hooks, 3.5 μl of purified grappling hook solution was applied onto copper EM grids (Cu 200 R 2/1, Quantifoil) and then automatically blotted from both sides using a Vitrobot Mark IV. Plunge-frozen grids were stored in liquid nitrogen.

Cryo-FIB milling

Lamellae through plunge-frozen *Aureispira-V. campbellii* mixture were obtained by automated sequential cryo-FIB milling as described previously (*31*). Briefly, EM grids were clipped into FIB milling autoloader-grids (Thermo Fisher Scientific) and mounted onto a 40° pretilted grid holder (*75*) (Leica Microsystems GmbH) using a VCM loading station (Leica Microsystems GmbH). For all grid transfers under cryo conditions, a VCT500 cryo-transfer system (Leica Microsystems GmbH) was used. Grids were sputter-coated with a ~4-nm-thick layer of tungsten using an ACE600 cryo-sputter coater (Leica Microsystems GmbH) and afterward transferred into a Crossbeam 550 FIB-SEM dual-beam instrument (Carl Zeiss Microscopy), equipped with a copper-band cooled mechanical cryo-stage (Leica Microsystems GmbH). The gas injection system (GIS) was used to deposit an organometallic platinum precursor layer onto each grid. Targeting of cells was done by scanning EM imaging (3 to 5 kV, 58 pA). Coordinates of chosen targets were saved in the stage navigator, and milling patterns were placed onto targets' FIB image (30 kV, 20 pA) using the SmartFIB software. To mill 10-μm-wide and ~250-nm-thick lamellae, a total of four currents were used, and currents were gradually reduced according to lamella thickness [rough milling (700, 300, and 100 pA) and polishing (50 pA)].

Cryo-ET

Micrographs of *Aureispira* samples were recorded on a Titan Krios 300 kV FEG transmission electron microscope (Thermo Fisher Scientific) equipped with a Quantum LS imaging filter (slit width 20 eV) and K2 direct electron detector (Gatan). A low magnification overview of the grid was recorded using SerialEM (*76*, *77*). Tilt series were collected automatically with SerialEM and covered an angular range from −50° to +70° or −60° to +60° with 2° increments for cryo-FIB–milled lamellae and *Aureispira* cells, respectively. The defocus was set to −8 μm for cryo-FIB–thinned lamellae and to −5 to −8 μm for intact *Aureispira* cells. The total dose of a tilt series accumulated 160 $e^-/Å^2$, and the pixel size at the specimen level was 3.46 Å. Cryo-ET data of *M. marina* were recorded on a Tecnai Polara 300kV TEM (FEI) equipped with post-column GIF 2002 imaging filter (slit width 20 eV) and K2 Summit direct electron detector (Gatan). Tilt series were collected from −60° to +60° with 1° increment at a pixel size of 4.9 Å using UCSF tomography (*78*) and with a defocus of −8 μm and a cumulative electron dose of 180 $e^-/Å^2$.

Tomogram reconstruction and subtomogram averaging

Tilt series were drift-corrected using alignframes. CTF correction and three-dimensional (3D) reconstructions were generated using the IMOD package (*79*, *80*). For visualization, tomograms were filtered using the tom_deconv deconvolution filter (*81*). The deep learning–based segmentation tool Dragonfly (*82*) was used for the segmentation of IsoNet-corrected (*83*) tomograms.

For subtomogram averaging of T6SS baseplates and transenvelope complexes, T6SSs were manually identified in individual tomograms, and their long axes were modeled in 3dmod (*80*) to generate model points and an initial motive list. Initial averages that were used as subsequent first references were created with PEET (*84*). Afterward, particles were extracted, aligned, and averaged with Dynamo (*85*). The 4 × 4–binned particles were aligned for 12 iterations (box size: 88 $pixels^3$). Afterward the datasets were split in half for gold-standard Fourier shell correlation (GSFSC) calculations, and masks focusing either on the baseplate or the transenvelope complex were used for alignments, respectively. Independent alignments were repeated for eight iterations using 2 × 2–binned tomograms (box size: 176 $pixels^3$). The set of particles was cleaned according to cross-correlation values, and another eight alignment iterations were performed followed by a final alignment with tight masks generated by Relion's mask generator (*86*). A total of 560 T6SSs were initially selected from 146 tomograms. The final CC-cleaned and C6-symmetrized average resulted from 399 baseplate particles and 334 transenvelope complex particles with a pixel size of 6.91 Å.

For subtomogram averaging of the extracellular antenna, 61 closed antennae and 21 open antennae were picked manually from tomograms using Dynamo for low-resolution averages serving as initial references. For the actual averaging run, the cropping points from the above T6SSs were now moved 65 pixels toward the extracellular space, and 4 × 4–binned particles containing both closed and open antennae were aligned for 12 iterations with either of the initial reference (box size: 120 $pixels^3$). The particles were separated into groups either containing closed antennae or open antennae according to cross-correlation values. The datasets were now averaged using the same processing steps as described above starting with half-datasets for FSC calculations and 2 × 2–binned subtomograms (box size: 240 $pixels^3$). The final C6-symmetrized averages resulted from 152 closed antenna particles and 76 open antennae particles with a pixel size of 6.91 Å.

For subtomogram averaging of the grappling hook distal end, the tips of the grappling hooks were manually picked from tomograms and averaged using the same Dynamo processing steps as outlined for the T6SS baseplate. The final C7-symmetrized average resulted from 425 grappling hooks particles (2 × 2–binned

with box size: 80 pixels^3) from 71 tomograms at a pixel size of 6.91 Å.

For subtomogram averaging of the grappling hook basal body, the particles were manually identified in individual tomograms, and their long axes from the OM toward the grappling hook distal ends were modeled in 3dmod (*80*) to generate model points and an initial motive list. An initial low-resolution average used as a subsequent reference was calculated with PEET with 72 particles (*84*). Afterward, particles were extracted, aligned, and averaged with Dynamo. The 4 × 4–binned particles were aligned for eight iterations (box size: 30 pixels^3). The refined table was then used for additional eight alignment iterations with a bigger particle box size (72 pixels^3). The final C7-symmetrized average resulted from 285 grappling hook basal body particles from 96 tomograms at a pixel size of 13.82 Å.

GSFSC curves for resolution estimation were calculated with Dynamo after alignment of the half-maps in UCSF Chimera (*87*) using the fit map function. No FSC curve was calculated for the grappling hook basal body, as it remained at low resolution.

Single-particle cryo-EM data collection and data processing

A total of 29,238 movies were collected on a Titan Krios G4 cryo-TEM (Thermo Fisher Scientific, ScopeM, Zürich) operated at 300 kV, equipped with a Bio-Continuum imaging filter (Gatan) and a K3 direct electron detector (Gatan). Automatic data collection was carried out using the Thermo Fisher Scientific EPU software. The scheme of four shots per hole was applied during data collection in counting mode, at a pixel size at specimen level of 1.065 Å/pixel and a defocus range of −1 to −2.5 µm. The total dose was 50 e^-/A^2 over 40 frames and 2-s exposure time.

The movies were motion-corrected using MotionCor2 (*88*). The resulting micrographs were imported into CryoSPARC v.4 (*89*), and the contrast transfer function (CTF) estimated using the patch CTF estimation tool. Grappling hook stem particles were picked manually, with a box size of 300 pixels, and averaged using 2D classification. The three best classes were then used as references for the filament tracer tool (filament diameter = 100 Å, interbox distance = 130 Å), which picked 2,452,192 particles. The particles were extracted with a box size of 300 Å, binned to a pixel size of 3.8 Å. During 2D classification, recentering after each iteration was not allowed, and a mask with a diameter of 90% of the box size was applied. After two rounds of classification and removal of bad classes, 1,309,380 particles of the stem remained.

The particles were subjected to helical refinement, using real-space windowing of 0.75 to 0.9 and a featureless cylinder with a diameter of 90 Å as reference. C7 symmetry was applied. The refinement was carried out without imposing helical symmetry. 3D classification, using real-space windowing of 0.75 to 0.9, was carried out with a target of five classes and a maximum resolution of 7 Å. The two classes with the most particles were refined individually. Particles were reextracted at a pixel size of 1.68 Å and subjected to helical refinement, applying a mask covering the central 50% of the map, 2D classification and 3D classification with a target resolution of 4 Å. A 50% mask was then applied to all other refinement jobs. An iterative process of 3D classifications, with a target resolution of 3.5 Å, helical refinement, nonuniform refinement (*90*), and global and local CTF refinement on unbinned particles resulted in six structures with resolutions between 3.4 and 3.7 Å. A graphical depiction of the workflow is shown in fig. S5.

For data processing of the grappling hook distal and proximal ends, terminal segments were identified visually from the filament tracer tool output and reextracted with a box size of 800 pixels and a binned pixel size of 4.26 Å, resulting in 78,681 particles. 2D classes were inspected manually and divided into two categories, referred to as "base" and "neck" classes, which were processed independently. C7 symmetry was applied in the refinement of both classes. Ab initio refinement was performed to obtain initial volumes, which were improved upon through an iterative process of 2D classification and homogeneous, nonuniform (*90*), and CTF refinement (all using the parameters described above). At the end of this process, the neck structure reached a global resolution of 3.77 Å, whereas the base structure reached 3.73 Å. A graphical depiction of the workflow is shown in fig. S6.

Global resolutions were determined by GSFSC, as estimated by CryoSPARC at a threshold of 0.143 (fig. S7). Local resolution was estimated at a GSFSC threshold of 0.143 across the entirety of the map and visualized in ChimeraX (*87*) (fig. S7). Finally, nonuniform refinement was run again on each of the final maps without imposing symmetry of any kind (C1). Unless stated otherwise, all data processing steps were carried out using the CryoSPARC v4 default settings. Noise was removed from the maps shown in figures using the "hide dust" tool in ChimeraX (*87*).

Structural modeling

The sharpened cryo-EM maps and the corresponding sequence in FASTA format were used as input for ModelAngelo 1.0 (*32*). The output models were inspected in ChimeraX (*87*), and the best-fitting protein chain was identified manually. The model was then manually curated and adjusted in Coot (*91*) [accessed through SBGrid (*92*)]. The models were then subjected to iterative real-space refinements against related density maps using RosettaCM (*93*). The final models were evaluated using "phenix.molprobity" (*94*) (table S10), and the correlations between models and the corresponding maps were estimated using "phenix.mtriage" (*94*). To analyze potential glycosylation sites, the cryo-EM density maps were masked with a 3-Å zone around the atomic model. This was used in Fig. 2J and fig. S9 to color all densities, which are more than 3 Å distant from the center axis of the atomic models in red. Molecular graphs were generated with Chimera (*95*) and ChimeraX .

Purification of T6SSs

For purification of *Aureispira* T6SSs, 50 ml *Aureispira* culture grown in ASWM was pelleted, resuspended in 3 ml of lysis buffer [150 mM NaCl, 50 mM Tris-HCl, 0.5× CellLytic B (Sigma-Aldrich), 1% Triton X-100, 200 µg/ml lysozyme, 50 µg/ml DNAse I, 1 mM phenylmethylsulfonyl fluoride, pH 7.4] and incubated at 37°C for 1 hour. Cell debris was removed by centrifugation (15,000*g*, 15 min, 4 °C), and cleared lysates were subjected to ultracentrifugation (150,000*g*, 1 hour, 4°C). Pellets were resuspended in 150 µl of resuspension buffer [150 mM NaCl, 50 mM Tris-HCl, supplemented with cOmplete EDTA-free protease inhibitor cocktail (Roche), pH 7.4]. For protein identification, the samples were sent to the Functional Genomic Center Zurich (FGCZ) for mass spectrometry analysis. A total of 100 µl of T6SS preparation was digested with 5 µl of trypsin (100 ng/µl in 10 mM HCl) and microwaved for 30 min at 60 °C. The sample was dried and dissolved in 20 µl of 0.1% formic acid, diluted 1:5, and transferred to the autosampler vials for liquid chromatography with tandem mass spectrometry analysis. A total of 1 µl was injected. Database searches were performed by importing the acquired mass spectrometry data into the PEAKS Studio (Bioinformatics solutions), and the data were searched against the NCBI protein database restricted to proteins from the *Aureispira* genus.

Negative-stain EM

Four microliters of sample solution was applied onto a glow-discharged, carbon-coated copper grid for 60 s, washed twice with water, and stained with 1% phosphotungstic acid for 20 s. The grids were examined using a Morgagni transmission electron microscope (Thermo Fisher Scientific) operated at 80 kV.

Whole-genome sequencing

Genomic DNA was extracted with Wizard Genomic DNA Purification Kit (Promega) from 1 ml of overnight *Aureispira* culture grown in ASWM. The DNA samples were sent to the Functional Genomic Center Zurich for long-read whole-genome sequencing.

One microgram of bacterial DNA for each derivative was used for PacBio library preparation

following PacBio protocol for multiplexing bacterial genomes for sequencing. The multiplexed PacBio libraries were further sequenced on a PacBio Sequel instrument using a single PacBio 1M SMRT cell, Sequel Binding Kit 3.0 and Sequencing Primer v4.

PacBio long reads were first demultiplexed using the "Demultiplex Barcodes" App in the PacBio Software SMRT Link (v 10.2.0.133434). Demultiplexed reads were then mapped to the reference genome (GCF_000724545.1_ Aureispira_sp._CCB-QB1), and small variants were identified using the "Resequencing" App in the SMRT Link. Variants were functionally annotated against the Aureispira_sp._CCB-QB1 gene models using SnpEff (v4.3). For large structural variant identification, demultiplexed reads were aligned to the reference genome using "pbmm2" in the SMRT Link command line tools (v 10.2.0.133434). Aligned reads were analyzed using "pbsv" in the same collection of SMRT Link command line tools for identification of large insertion, deletion, inversion, translocation, and duplication.

De novo assembly was performed using Canu (v2.0) and the "Microbial Assembly" App in SMRT Link (v 10.2.0.133434). Assembled contigs were compared with the reference genome using nucmer and dnadiff in MUMmer (v4.0.0beta2).

Stable isotope probing—single-cell Raman microspectroscopy

To investigate the uptake of *V. campbellii* components by *Aureispira*, the stable isotope probing (SIP)–Raman technique was used. To label prey cells with deuterium (D), *V. campbellii* cells were cultured in 50% D_2O-containing ASWM overnight and subsequently subcultured in 50% D_2O-containing L-ASWM for 2 hours. The same procedures were repeated with *V. campbellii* cells cultured in conventional H_2O ASWM or L-ASWM, to be used as unlabeled control. All *V. campbellii* cells were washed once with H_2O L-ASWM before mixing with an overnight *Aureispira* culture, which was starved in L-ASWM for 2 hours. The *Aureispira*–*V. campbellii* 1-to-1 mixture was then cocultured at 30°C with 200 rpm for 1 hour. A 5-μl droplet containing each sample was placed on an aluminum-coated slide (EMF Corp., USA) and dried at 30°C for 10 min. The samples were then washed using Milli-Q (MQ) water to remove traces of the medium, followed by air blowing to remove residual MQ water (*46*).

The samples were measured using a confocal Raman microspectroscope (LabRAM HR Evolution, Horiba Scientific, France). The system is based on an upright microscope (BxFM, Olympus) integrated with components for Raman measurements, including an objective (MPlan N 100×, 0.90 NA, Olympus), a 100-μm confocal pinhole, a 300-lines/mm diffraction grating (blazed at 600 nm), and a spectrometer (back illuminated deep-depleted CCD; 1024 pixels by 256 pixels). A 532-nm laser at 10 mW (continuous wave neodymium-doped yttrium aluminum garnet; CW Nd: YAG) was illuminated onto the individual cells, and their Raman spectra were measured with 10-s exposure time.

The measured Raman spectra were processed using a code built in-house (*46*). Smoothing (de-noising) and baseline subtraction were conducted using the Savitzky-Golay filter (polynomial order and frame length: 3 and 9) and a polynomial-based algorithm (polynomial order and threshold: 1 and 0.001), respectively. To evaluate the deuterium labeling status of *Aureispira*, the Raman intensity for the carbon-deuterium peak (C-D at 2100 to 2300 cm^{-1}; integrated intensity, $I_{2100–2300}$) was normalized by that for a lipid peak (C-H at 2800 to 3100 cm^{-1}; integrated intensity, $I_{2800–3100}$). The C-H peak, a proxy for cell biomass, was used for this normalization to consider the heterogeneity of biomass between cells and to compensate the precision difference of the focus of the Raman laser beam on individual cells

$$C-D/C-H = I_{2100-2300cm^{-1}}/I_{2800-3100cm^{-1}}$$

where *I* represents integrated intensity within a specified spectral region.

RNA isolation and quantitative reverse transcription PCR (qRT-PCR)

An *Aureispira* overnight culture was subcultured into artificial seawater medium without any nutrients (0-ASWM) [2.4% Instant Ocean (Aquarium Systems), 10 mM HEPES, pH 7.6] or ASWM for 6 hours. One milliliter of bacterial cell culture was pelleted, and the total RNA was extracted with the SPLIT RNA extraction kit (Lexogen) followed by DNase treatment with the TURBO DNase kit (Thermo Fisher). One microgram of the RNA was reverse transcribed into cDNA with the iScript Advanced cDNA Synthesis kit (Bio-rad). Twenty microliters of the end products were diluted by adding 180 μl nuclease-free water and stored at −20°C until further analysis.

Five microliters of each sample was used for qRT-PCR. cDNA samples were mixed with 10 μl of KAPA SYBR FAST (KAPA Biosystems) and 2.5 μl of 5 μM forward primer and reverse primer. The qRT-PCR was done in CFX96 Real-Time System C1000 Touch Thermal Cycler (Bio-Rad). The cycling program was as follows: one cycle of 95°C for 5 min, 40 cycles of 95°C for 10 s, 62°C for 10 s, 72°C for 12 s, followed by a melt curve. For each experiment, three technical replicates were conducted and repeated with three biological replicates. Data processing and relative gene expression were calculated with Bio-Rad CFX Maestro (Bio-Rad).

Evaluation of ISs excision upon starvation

The 50 ml *Aureispira* overnight culture in ASWM was pelleted and resuspended in 50 ml 0-ASWM. On the same day, 50 ml *V. campbellii* overnight cultures in ASWM were pelleted, resuspended in 2 ml 0-ASWM, and added to each *Aureispira* 0-ASWM culture. The OD_{600} of each culture was measured every day, and OD_{600} was adjusted to 2 by the addition of *V. campbellii* cells. PCR was performed after the T6SS-negative derivatives showed a decreased OD_{600}. Bands from the PCR products were cut out after agarose gel electrophoreses, purified, and sent to Microsynth AG for Sanger sequencing to confirm the excision of the ISs.

Metagenomic abundance analysis

Sea surface water was collected from Canoe Cove, Nahant, Massachusetts, USA (Lat: 42°25′10.6″N, Lon: 70°54′24.2″W), from 23 July (Julian day 204) to 23 October 2010 (Julian day 296) (*47*).

The amplicon reads (SRR5175890 to SRR5175997 and SRR5176042 to SRR5176255) were previously determined and analyzed following the methods described in (*47*). Coupled dynamics were analyzed by determining the Pearson correlation coefficient for the relative abundance of each amplified sequence variant of the *Saprospiraceae* and *Vibrionaceae* on each day of the Nahant time series, taking into account time-lagged correlations due to predator-prey dynamic by smoothing the abundance data by a rolling average over 7 days. The threshold for significance of correlations was set to 0.03. The difference between the smoothed and direct correlation coefficient was determined, and the 95th percentile calculated. Every correlation above this threshold was stated as significant. To validate correlations, the values for the *Vibrionaceae* abundance were 1000 times permuted, and for each permutation, the Pearson correlation coefficient and the *P* value were determined and their mean calculated. In addition, the number of correlations above the previous determined 95th percentile per 1000 permutations and *P* values greater than 0.03 per 1000 permutations were calculated.

The DNA used for amplicon preparation was also used for metagenomic sequencing. A subset of samples (Julian days 231, 235, 237, 239, 241, 243, and 247) were library prepped and sequenced by the BioMicroCenter (MIT, Cambridge, MA) on an Illumina NextSeq flowcell. Samples of each day were library prepped and sequenced by the BioMicroCenter (MIT, Cambridge, MA) using an Illumina NovaSeq S1flowcell.

The relative abundances of genomes were determined as follows: Reads were (i) cleaned of phiX with bowtie2 (v. 2.3.4.2) (*96*) and quality trimmed with trimgalore (v.0.5.0) (https://github.com/FelixKrueger/TrimGalore) with the

parameters "-e 0.05–clip_R1 1–clip_R2 1–three_prime_clip_R1 1–three_prime_clip_R2 1–length 70–stringency 1–paired–max_n 1–phred33." (ii) Error correction was done with Tadpole (v. 38.18, BBTools package; https://jgi.doe.gov/data-and-tools/software-tools/bbtools/). (iii) Reads were filtered using kraken2 (v.2.1.3) (*97*) classification (bacteria and archaea). (iv) Mapping was performed with bbmap (v.39.01) (BBTools package) to genomes with the parameters "fast=t minid=0.95 idfilter=0.98" and results sorted with samtools (*98*).

For prey relative abundance, the reads were mapped to all available RefSeq genomes of the *Vibrionaceae* (218, NCBI, Nov. 2023) and summed. For the ixotrophy-positive strains, *Saprospira grandis* str. Lewin (GCF_000250635.1), *Aureispira* sp. CCB-QB1 (GCF_000724545.1), *Saprospira* sp. CCB-QB6 (GCF_028464065.1), and *Aureispira* sp. CCB-E (GCF_031326345.1) were analyzed and as control the ixotrophy-negative strain *A. machipongonensis* (GCF_000166275.1). Plots were done with RStudio and smoothed by a rolling average of 3. The source data of the used metagenomes can be found in data S2.

REFERENCES AND NOTES

1. T. Fenchel, Microbial behavior in a heterogeneous world. *Science* **296**, 1068–1071 (2002). doi: 10.1126/science.1070118; pmid: 12004118
2. R. Stocker, Marine microbes see a sea of gradients. *Science* **338**, 628–633 (2012). doi: 10.1126/science.1208929; pmid: 23118182
3. S. Thiery, C. Kaimer, The predation strategy of *Myxococcus xanthus*. *Front. Microbiol.* **11**, 2 (2020). doi: 10.3389/fmicb.2020.00002; pmid: 32010119
4. G. Laloux, Shedding light on the cell biology of the predatory bacterium *Bdellovibrio bacteriovorus*. *Front. Microbiol.* **10**, 3136 (2020). doi: 10.3389/fmicb.2019.03136; pmid: 32038570
5. E. Bratanis, T. Andersson, R. Lood, E. Bukowska-Faniband, Biotechnological potential of *Bdellovibrio* and like organisms and their secreted enzymes. *Front. Microbiol.* **11**, 662 (2020). doi: 10.3389/fmicb.2020.00662; pmid: 32351487
6. T. Shiratori, S. Suzuki, Y. Kakizawa, K. I. Ishida, Phagocytosis-like cell engulfment by a planctomycete bacterium. *Nat. Commun.* **10**, 5529 (2019). doi: 10.1038/s41467-019-13499-2; pmid: 31827088
7. D. Moreira, Y. Zivanovic, A. I. López-Archilla, M. Iniesto, P. López-García, Reductive evolution and unique predatory mode in the CPR bacterium *Vampirococcus lugosii*. *Nat. Commun.* **12**, 2454 (2021). doi: 10.1038/s41467-021-22762-4; pmid: 33911080
8. R. A. Lewin, *Saprospira grandis*: A flexibacterium that can catch bacterial prey by "ixotrophy". *Microb. Ecol.* **34**, 232–236 (1997). doi: 10.1007/s002489900052; pmid: 9337418
9. G. Furusawa, P. L. Hartzell, V. Navaratnam, Calcium is required for ixotrophy of *Aureispira* sp. CCB-QB1. *Microbiology (Reading)* **161**, 1933–1941 (2015). doi: 10.1099/mic.0.000158; pmid: 26306656
10. M. Shi *et al*., A novel bacterium *Saprospira* sp. strain PdY3 forms bundles and lyses cyanobacteria. *Front. Biosci.* **11**, 1916–1923 (2006). doi: 10.2741/1934; pmid: 16368567
11. P. J. Ashton, R. D. Robarts, Apparent predation of *Microcystis aeruginosa* Kütz. Emend Elenkin by a *Saprospira*-like bacterium in a hypertrophic lake (Hartbeespoort Dam, South Africa). *South Afr. J. Aquat. Sci.* **13**, 44–47 (1987). doi: 10.1080/03779688.1987.9634542
12. G. Furusawa, T. Yoshikawa, A. Yasuda, T. Sakata, Algicidal activity and gliding motility of *Saprospira* sp. SS98-5. *Can. J. Microbiol.* **49**, 92–100 (2003). doi: 10.1139/w03-017; pmid: 12718397
13. M. Svercel, B. Saladin, S. J. van Moorsel, S. Wolf, H. C. Bagheri, Antagonistic interactions between filamentous heterotrophs and the cyanobacterium *Nostoc muscorum*. *BMC Res. Notes* **4**, 357 (2011). doi: 10.1186/1756-0500-4-357; pmid: 21914201
14. D. L. Correll, R. A. Lewin, Rod-shaped ribonucleoprotein particles from Saprospira. *Can. J. Microbiol.* **10**, 63–74 (1964). doi: 10.1139/m64-010; pmid: 14124863
15. R. A. Lewin, J. Kiethe, Formation of rhapidosomes in Saprospira. *Can. J. Microbiol.* **11**, 935–938 (1965). doi: 10.1139/m65-124; pmid: 5879505
16. G. Furusawa *et al*., Characterization of cytoplasmic fibril structures found in gliding cells of *Saprospira* sp. *Can. J. Microbiol.* **51**, 875–880 (2005). doi: 10.1139/w05-081; pmid: 16333347
17. M. Basler, M. Pilhofer, G. P. Henderson, G. J. Jensen, J. J. Mekalanos, Type VI secretion requires a dynamic contractile phage tail-like structure. *Nature* **483**, 182–186 (2012). doi: 10.1038/nature10846; pmid: 22367545
18. N. J. Shikuma *et al*., Marine tubeworm metamorphosis induced by arrays of bacterial phage tail-like structures. *Science* **343**, 529–533 (2014). doi: 10.1126/science.1246794; pmid: 24407482
19. A. Desfosses *et al*., Atomic structures of an entire contractile injection system in both the extended and contracted states. *Nat. Microbiol.* **4**, 1885–1894 (2019). doi: 10.1038/s41564-019-0530-6; pmid: 31384001
20. D. Böck *et al*., In situ architecture, function, and evolution of a contractile injection system. *Science* **357**, 713–717 (2017). doi: 10.1126/science.aan7904; pmid: 28818949
21. G. L. Weiss *et al*., Structure of a thylakoid-anchored contractile injection system in multicellular cyanobacteria. *Nat. Microbiol.* **7**, 386–396 (2022). doi: 10.1038/s41564-021-01055-y; pmid: 35165386
22. J. Xu *et al*., Identification and structure of an extracellular contractile injection system from the marine bacterium *Algoriphagus machipongonensis*. *Nat. Microbiol.* **7**, 397–410 (2022). doi: 10.1038/s41564-022-01059-2; pmid: 35165385
23. F. Jiang *et al*., Cryo-EM structure and assembly of an extracellular contractile injection system. *Cell* **177**, 370–383. e15 (2019). doi: 10.1016/j.cell.2019.02.020; pmid: 30905475
24. Y. R. Brunet, A. Zoued, F. Boyer, B. Douzi, E. Cascales, The type VI secretion TssEFGK-VgrG phage-like baseplate is recruited to the TssJLM membrane complex via multiple contacts and serves as assembly platform for tail tube/sheath polymerization. *PLOS Genet.* **11**, e1005545 (2015). doi: 10.1371/journal.pgen.1005545; pmid: 26460929
25. C. Rapisarda *et al*., *In situ* and high-resolution cryo-EM structure of a bacterial type VI secretion system membrane complex. *EMBO J.* **38**, e100886 (2019). doi: 10.15252/embj.2018100886; pmid: 30877094
26. G. Furusawa, N.-S. Lau, A. C. Shu-Chien, A. Jaya-Ram, A.-A. A. Amirul, Identification of polyunsaturated fatty acid and diterpenoid biosynthesis pathways from draft genome of *Aureispira* sp. CCB-QB1. *Mar. Genomics* **19**, 39–44 (2015). doi: 10.1016/j.margen.2014.10.006; pmid: 25468060
27. H. I. Yeoh *et al*., The *Vibrio*-predatory filamentous bacteria effectively removed acute hepatopancreatic necrosis disease (AHPND) causative *Vibrio parahaemolyticus* in vitro. *Aquacult. Rep.* **21**, 100910 (2021). doi: 10.1016/j.aqrep.2021.100910
28. S. S. Nelson, S. Bollampalli, M. J. McBride, SprB is a cell surface component of the *Flavobacterium johnsoniae* gliding motility machinery. *J. Bacteriol.* **190**, 2851–2857 (2008). doi: 10.1128/JB.01904-07; pmid: 18281397
29. M. Marko, C. Hsieh, R. Schalek, J. Frank, C. Mannella, Focused-ion-beam thinning of frozen-hydrated biological specimens for cryo-electron microscopy. *Nat. Methods* **4**, 215–217 (2007). doi: 10.1038/nmeth1014; pmid: 17277781
30. A. Rigort, J. M. Plitzko, Cryo-focused-ion-beam applications in structural biology. *Arch. Biochem. Biophys.* **581**, 122–130 (2015). doi: 10.1016/j.abb.2015.02.009; pmid: 25703192
31. T. Zachs *et al*., Fully automated, sequential focused ion beam milling for cryo-electron tomography. *eLife* **9**, e52286 (2020). doi: 10.7554/eLife.52286; pmid: 32149604
32. K. Jamali *et al*., Automated model building and protein identification in cryo-EM maps. *Nature* **628**, 450–457 (2024). doi: 10.1038/s41586-024-07215-4; pmid: 38408488
33. M. J. Coyne *et al*., Phylum-wide general protein O-glycosylation system of the Bacteroidetes. *Mol. Microbiol.* **88**, 772–783 (2013). doi: 10.1111/mmi.12220; pmid: 23551589
34. P. D. Veith, D. G. Gorasia, E. C. Reynolds, Characterization of the *O*-glycoproteome of *Flavobacterium johnsoniae*. *J. Bacteriol.* **205**, e00093-23 (2023). doi: 10.1128/jb.00093-23; pmid: 37162352
35. D. G. Gorasia *et al*., Type B CTD proteins secreted by the type IX secretion system associate with PorP-like proteins for cell surface anchorage. *Int. J. Mol. Sci.* **23**, 5681 (2022). doi: 10.3390/ijms23105681; pmid: 35628493
36. Y. W. Chang, L. A. Rettberg, D. R. Ortega, G. J. Jensen, *In vivo* structures of an intact type VI secretion system revealed by electron cryotomography. *EMBO Rep.* **18**, 1090–1099 (2017). doi: 10.15252/embr.201744072; pmid: 28487352
37. T. R. Bongiovanni *et al*., Assembly of a unique membrane complex in type VI secretion systems of Bacteroidota. *Nat. Commun.* **15**, 429 (2024). doi: 10.1038/s41467-023-44426-1; pmid: 38200008
38. S. Pukatzki, A. T. Ma, A. T. Revel, D. Sturtevant, J. J. Mekalanos, Type VI secretion system translocates a phage tail spike-like protein into target cells where it cross-links actin. *Proc. Natl. Acad. Sci. U.S.A.* **104**, 15508–15513 (2007). doi: 10.1073/pnas.0706532104; pmid: 17873062
39. R. E. Hernandez, R. Gallegos-Monterrosa, S. J. Coulthurst, Type VI secretion system effector proteins: Effective weapons for bacterial competitiveness. *Cell. Microbiol.* **22**, e13241 (2020). doi: 10.1111/cmi.13241; pmid: 32592518
40. A. Vettiger, M. Basler, Type VI secretion system substrates are transferred and reused among sister cells. *Cell* **167**, 99–110.e12 (2016). doi: 10.1016/j.cell.2016.08.023; pmid: 27616061
41. P. Siguier, E. Gourbeyre, M. Chandler, Bacterial insertion sequences: Their genomic impact and diversity. *FEMS Microbiol. Rev.* **38**, 865–891 (2014). doi: 10.1111/1574-6976.12067; pmid: 24499397
42. M. Kusumoto *et al*., Insertion sequence-excision enhancer removes transposable elements from bacterial genomes and induces various genomic deletions. *Nat. Commun.* **2**, 152 (2011). doi: 10.1038/ncomms1152; pmid: 21224843
43. P. A. Calvo, V. Mateo-Cáceres, S. Díaz-Arco, M. Redrejo-Rodríguez, M. de Vega, The enterohemorrhagic *Escherichia coli* insertion sequence-excision enhancer protein is a DNA polymerase with microhomology-mediated end-joining activity. *Nucleic Acids Res.* **51**, 1189–1207 (2023). doi: 10.1093/nar/gkad017; pmid: 36715333
44. A. K. Sinha, C. Possoz, D. R. F. Leach, The roles of bacterial DNA double-strand break repair proteins in chromosomal DNA replication. *FEMS Microbiol. Rev.* **44**, 351–368 (2020). doi: 10.1093/femsre/fuaa009; pmid: 32286623
45. C. J. Dorman, "Conservation and evolution of the dynamic genome" in *Structure and Function of the Bacterial Genome* (Wiley, 2020), pp. 67–112.
46. K. S. Lee *et al*., Raman microspectroscopy for microbiology. *Nat. Rev. Methods Primers* **1**, 80 (2021). doi: 10.1038/s43586-021-00075-6
47. A. M. Martin-Platero *et al*., High resolution time series reveals cohesive but short-lived communities in coastal plankton. *Nat. Commun.* **9**, 266 (2018). doi: 10.1038/s41467-017-02571-4; pmid: 29348571
48. R. A. Alegado *et al*., *Algoriphagus machipongonensis* sp. nov., co-isolated with a colonial choanoflagellate. *Int. J. Syst. Evol. Microbiol.* **63**, 163–168 (2013). doi: 10.1099/ijs.0.038646-0; pmid: 22368173
49. S. C. Booth, O. J. Meacock, K. R. Foster, Cell motility empowers bacterial contact weapons. *ISME J.* 10.1093/ismejo/wrae141 (2024). doi: 10.1093/ismejo/wrae141; pmid: 39073907
50. C. Moissl, R. Rachel, A. Briegel, H. Engelhardt, R. Huber, The unique structure of archaeal 'hami', highly complex cell appendages with nano-grappling hooks. *Mol. Microbiol.* **56**, 361–370 (2005). doi: 10.1111/j.1365-2958.2005.04294.x; pmid: 15813730
51. A. J. Probst *et al*., Biology of a widespread uncultivated archaeon that contributes to carbon fixation in the subsurface. *Nat. Commun.* **5**, 5497 (2014). doi: 10.1038/ncomms6497; pmid: 25425419
52. A. K. Perras *et al*., S-layers at second glance? Altiarchaeal grappling hooks (hami) resemble archaeal S-layer proteins in structure and sequence. *Front. Microbiol.* **6**, 543 (2015). doi: 10.3389/fmicb.2015.00543; pmid: 26106369
53. S. G. Caulton *et al*., *Bdellovibrio bacteriovorus* uses chimeric fibre proteins to recognize and invade a broad range of bacterial hosts. *Nat. Microbiol.* **9**, 214–227 (2024). doi: 10.1038/s41564-023-01552-2; pmid: 38177296
54. S. B. Otto, R. Servajean, A. Lemopoulos, A.-F. Bitbol, M. Blokesch, Interactions between pili affect the outcome of bacterial competition driven by the type VI secretion system. *Curr. Biol.* **34**, 2403–2417.e9 (2024). doi: 10.1016/j.cub.2024.04.041; pmid: 38749426
55. M. Hall, S. Nylander, H. F. Jenkinson, K. Persson, Structure of the C-terminal domain of AspA (antigen I/II-family) protein from *Streptococcus pyogenes*. *FEBS Open Bio* **4**, 283–289 (2014). doi: 10.1016/j.fob.2014.02.012; pmid: 24918040

56. J. Liu, M. J. McBride, S. Subramaniam, Cell surface filaments of the gliding bacterium *Flavobacterium johnsoniae* revealed by cryo-electron tomography. *J. Bacteriol.* **189**, 7503–7506 (2007). doi: 10.1128/JB.00957-07; pmid: 17693495
57. D. Nakane, K. Sato, H. Wada, M. J. McBride, K. Nakayama, Helical flow of surface protein required for bacterial gliding motility. *Proc. Natl. Acad. Sci. U.S.A.* **110**, 11145–11150 (2013). doi: 10.1073/pnas.1219753110; pmid: 23781102
58. T. E. Wood *et al*., The *Pseudomonas aeruginosa* T6SS delivers a periplasmic toxin that disrupts bacterial cell morphology. *Cell Rep.* **29**, 187–201.e7 (2019). doi: 10.1016/j.celrep.2019.08.094; pmid: 31577948
59. A. M. Geller *et al*., The extracellular contractile injection system is enriched in environmental microbes and associates with numerous toxins. *Nat. Commun.* **12**, 3743 (2021). doi: 10.1038/s41467-021-23777-7; pmid: 34145238
60. J. C. Whitney *et al*., Identification, structure, and function of a novel type VI secretion peptidoglycan glycoside hydrolase effector-immunity pair. *J. Biol. Chem.* **288**, 26616–26624 (2013). doi: 10.1074/jbc.M113.488320; pmid: 23878199
61. C. Whiteway *et al*., Scarless excision of an insertion sequence restores capsule production and virulence in *Acinetobacter baumannii*. *ISME J.* **16**, 1473–1477 (2022). doi: 10.1038/s41396-021-01179-3; pmid: 34949784
62. K. Nakamura *et al*., Insertion sequence (IS)-excision enhancer (IEE)-mediated IS excision from the *lacZ* gene restores the lactose utilization defect of shiga toxin-producing *Escherichia coli* O121:H19 strains and is responsible for their delayed lactose utilization phenotype. *Appl. Environ. Microbiol.* **88**, e00760-22 (2022). doi: 10.1128/aem.00760-22; pmid: 35913153
63. J. Nesper, D. Kapfhammer, K. E. Klose, H. Merkert, J. Reidl, Characterization of *Vibrio cholerae* O1 antigen as the bacteriophage K139 receptor and identification of IS*1004* insertions aborting O1 antigen biosynthesis. *J. Bacteriol.* **182**, 5097–5104 (2000). doi: 10.1128/JB.182.18.5097-5104.2000; pmid: 10960093
64. N. C. Drebes Dörr *et al*., Single nucleotide polymorphism determines constitutive versus inducible type VI secretion in *Vibrio cholerae*. *ISME J.* **16**, 1868–1872 (2022). doi: 10.1038/s41396-022-01234-7; pmid: 35411099
65. A. N. Septer, G. Sharpe, E. A. Shook, The *Vibrio fischeri* type VI secretion system incurs a fitness cost under host-like conditions. bioRxiv 2023.03.07.529561 [Preprint] (2023); https://doi.org/10.1101/2023.03.07.529561.
66. A. I. Perault *et al*., Host adaptation predisposes *Pseudomonas aeruginosa* to type vi secretion system-mediated predation by the *Burkholderia cepacia* complex. *Cell Host Microbe* **28**, 534–547.e3 (2020). doi: 10.1016/j.chom.2020.06.019; pmid: 32755549
67. S. Robitaille *et al*., Community composition and the environment modulate the population dynamics of type VI secretion in human gut bacteria. *Nat. Ecol. Evol.* **7**, 2092–2107 (2023). doi: 10.1038/s41559-023-02230-6; pmid: 37884689
68. Y. Kanai, S. Tsuru, C. Furusawa, Experimental demonstration of operon formation catalyzed by insertion sequence. *Nucleic Acids Res.* **50**, 1673–1686 (2022). doi: 10.1093/nar/gkac004; pmid: 35066585
69. J. Schindelin *et al*., Fiji: An open-source platform for biological-image analysis. *Nat. Methods* **9**, 676–682 (2012). doi: 10.1038/nmeth.2019; pmid: 22743772
70. C. A. Simpson, R. Podicheti, D. B. Rusch, A. B. Dalia, J. C. van Kessel, Diversity in natural transformation frequencies and regulation across *Vibrio* species. *mBio* **10**, e02788-19 (2019). doi: 10.1128/mBio.02788-19; pmid: 31848285
71. G. C. Yang, G. D. Schrank, B. A. Freeman, Purification of flagellar cores of *Vibrio cholerae*. *J. Bacteriol.* **129**, 1121–1128 (1977). doi: 10.1128/jb.129.2.1121-1128.1977; pmid: 838680
72. M. C. Gaines *et al*., Electron cryo-microscopy reveals the structure of the archaeal thread filament. *Nat. Commun.* **13**, 7411 (2022). doi: 10.1038/s41467-022-34652-4; pmid: 36456543
73. W. F. Tivol, A. Briegel, G. J. Jensen, An improved cryogen for plunge freezing. *Microsc. Microanal.* **14**, 375–379 (2008). doi: 10.1017/S1431927608080781; pmid: 18793481
74. C. V. Iancu *et al*., Electron cryotomography sample preparation using the Vitrobot. *Nat. Protoc.* **1**, 2813–2819 (2006). doi: 10.1038/nprot.2006.432; pmid: 17406539
75. J. M. Medeiros *et al*., Robust workflow and instrumentation for cryo-focused ion beam milling of samples for electron cryotomography. *Ultramicroscopy* **190**, 1–11 (2018). doi: 10.1016/j.ultramic.2018.04.002; pmid: 29655973
76. D. N. Mastronarde, Automated electron microscope tomography using robust prediction of specimen movements. *J. Struct. Biol.* **152**, 36–51 (2005). doi: 10.1016/j.jsb.2005.07.007; pmid: 16182563
77. M. Schorb, I. Haberbosch, W. J. H. Hagen, Y. Schwab, D. N. Mastronarde, Software tools for automated transmission electron microscopy. *Nat. Methods* **16**, 471–477 (2019). doi: 10.1038/s41592-019-0396-9; pmid: 31086343
78. S. Q. Zheng *et al*., UCSF tomography: An integrated software suite for real-time electron microscopic tomographic data collection, alignment, and reconstruction. *J. Struct. Biol.* **157**, 138–147 (2007). doi: 10.1016/j.jsb.2006.06.005; pmid: 16904341
79. J. R. Kremer, D. N. Mastronarde, J. R. McIntosh, Computer visualization of three-dimensional image data using IMOD. *J. Struct. Biol.* **116**, 71–76 (1996). doi: 10.1006/jsbi.1996.0013; pmid: 8742726
80. D. N. Mastronarde, Correction for non-perpendicularity of beam and tilt axis in tomographic reconstructions with the IMOD package. *J. Microsc.* **230**, 212–217 (2008). doi: 10.1111/j.1365-2818.2008.01977.x; pmid: 18445149
81. D. Tegunov, P. Cramer, Real-time cryo-electron microscopy data preprocessing with Warp. *Nat. Methods* **16**, 1146–1152 (2019). doi: 10.1038/s41592-019-0580-y; pmid: 31591575
82. J. E. Heebner *et al*., Deep learning-based segmentation of cryo-electron tomograms. *J. Vis. Exp.* **2022**, e64435 (2022). doi: 10.3791/64435-v; pmid: 36440884
83. Y.-T. Liu *et al*., Isotropic reconstruction for electron tomography with deep learning. *Nat. Commun.* **13**, 6482 (2022). doi: 10.1038/s41467-022-33957-8; pmid: 36309499
84. D. Nicastro *et al*., The molecular architecture of axonemes revealed by cryoelectron tomography. *Science* **313**, 944–948 (2006). doi: 10.1126/science.1128618; pmid: 16917055
85. D. Castaño-Díez, M. Kudryashev, M. Arheit, H. Stahlberg, Dynamo: A flexible, user-friendly development tool for subtomogram averaging of cryo-EM data in high-performance computing environments. *J. Struct. Biol.* **178**, 139–151 (2012). doi: 10.1016/j.jsb.2011.12.017; pmid: 22245546
86. J. Zivanov *et al*., New tools for automated high-resolution cryo-EM structure determination in RELION-3. *eLife* **7**, e42166 (2018). doi: 10.7554/eLife.42166; pmid: 30412051
87. E. F. Pettersen *et al*., UCSF ChimeraX: Structure visualization for researchers, educators, and developers. *Protein Sci.* **30**, 70–82 (2021). doi: 10.1002/pro.3943; pmid: 32881101
88. S. Q. Zheng *et al*., MotionCor2: Anisotropic correction of beam-induced motion for improved cryo-electron microscopy. *Nat. Methods* **14**, 331–332 (2017). doi: 10.1038/nmeth.4193; pmid: 28250466
89. A. Punjani, J. L. Rubinstein, D. J. Fleet, M. A. Brubaker, cryoSPARC: Algorithms for rapid unsupervised cryo-EM structure determination. *Nat. Methods* **14**, 290–296 (2017). doi: 10.1038/nmeth.4169; pmid: 28165473
90. A. Punjani, H. Zhang, D. J. Fleet, Non-uniform refinement: Adaptive regularization improves single-particle cryo-EM reconstruction. *Nat. Methods* **17**, 1214–1221 (2020). doi: 10.1038/s41592-020-00990-8; pmid: 33257830
91. P. Emsley, B. Lohkamp, W. G. Scott, K. Cowtan, Features and development of *Coot*. *Acta Crystallogr. D Biol. Crystallogr.* **66**, 486–501 (2010). doi: 10.1107/S0907444910007493; pmid: 20383002
92. A. Morin *et al*., Collaboration gets the most out of software. *eLife* **2**, e01456 (2013). doi: 10.7554/eLife.01456; pmid: 24040512
93. Y. Song *et al*., High-resolution comparative modeling with RosettaCM. *Structure* **21**, 1735–1742 (2013). doi: 10.1016/j.str.2013.08.005; pmid: 24035711
94. P. D. Adams *et al*., *PHENIX*: A comprehensive Python-based system for macromolecular structure solution. *Acta Crystallogr. D Biol. Crystallogr.* **66**, 213–221 (2010). doi: 10.1107/S0907444909052925; pmid: 20124702
95. E. F. Pettersen *et al*., UCSF Chimera—A visualization system for exploratory research and analysis. *J. Comput. Chem.* **25**, 1605–1612 (2004). doi: 10.1002/jcc.20084; pmid: 15264254
96. B. Langmead, S. L. Salzberg, Fast gapped-read alignment with Bowtie 2. *Nat. Methods* **9**, 357–359 (2012). doi: 10.1038/nmeth.1923; pmid: 22388286
97. D. E. Wood, J. Lu, B. Langmead, Improved metagenomic analysis with Kraken 2. *Genome Biol.* **20**, 257 (2019). doi: 10.1186/s13059-019-1891-0; pmid: 31779668
98. P. Danecek *et al*., Twelve years of SAMtools and BCFtools. *Gigascience* **10**, giab008 (2021). doi: 10.1093/gigascience/giab008; pmid: 33590861

ACKNOWLEDGMENTS

ScopeM is acknowledged for instrument access at ETH Zürich. We thank O. Medalia for access to the Polara microscope at the University of Zürich. Functional Genomic Center Zurich is acknowledged for technical support. We thank T. Zachs for the help with cryo-FIB milling. We thank F. Wollweber for help with light microscopy and segmentation of the cryo-tomograms. We thank M. Peterek for technical support. We thank P. Afanasyev, D. Boehringer, B. Qureshi, and D. Wang for their help with single-particle cryo-EM. We thank J. J. L. Malit for help with bioinformatics analysis. C. Ericson is acknowledged for the help with sucrose gradient purification. We thank L. M. L. Keller for the help with qPCR. W.-D. Hardt, B. Nguyen, and M. Horn are acknowledged for insightful discussions. We thank S.-V. Albers and S. Sivabalasarma for suggestions on grappling hook purifications. **Funding:** Swiss National Science Foundation 310030_212592 (M.P.), European Research Council 679209 and 101000232 (M.P.), NOMIS Foundation (M.P.), Gordon and Betty Moore Foundation Symbiosis in Aquatic Systems Initiative Investigator Award GBMF9197 (R.S.), Simons Foundation Principles of Microbial Ecosystems (PriME) Collaborative 542395 (R.S.), Swiss National Science Foundation 315230_176189 (RS), National Centre of Competence in Research (NCCR) Microbiomes 51NF40_180575 (R.S.), and Simons Foundation Life Sciences Project Award-572792 (N.B. and M.F.P.). **Author contributions:** Y.-W.L. conducted all experiments that included light microscopy, killing assays, cryo-FIB milling, cryo-ET, qRT-PCR, and characterization of IS excision. G.L.W. generated preliminary data and assisted with cryo-FIB, cryo-ET, and subtomogram averaging. With support from Y.-W.L. and J.X., D.A. established the purification of grappling hooks, processed the cryo-EM data, built an initial atomic model, and analyzed the structures. Raman microspectroscopy and data analysis were performed by K.S.L. in the lab of R.S. N.B. and M.F.P. analyzed the time-resolved metagenomic dataset. G.F. shared the initial *Aureispira* culture and gave feedback during discussions. Y.-W.L., G.L.W., and M.P. wrote the manuscript, with comments from all authors. **Competing interests:** R.S. serves as chief scientific officer at PhAST Diagnostics. This company is unrelated to the subject matter of this manuscript. **Data and materials availability:** Example tomograms (EMD-50531, EMD-50533, EMD-50544, EMD-50548, and EMD-50551), subtomogram averages (EMD-50554 to EMD-50558), and cryo-EM maps (EMD-50537 to EMD-50543, and EMD-51127) were uploaded to the Electron Microscopy Data Bank. Atomic coordinates of the grappling hook models were uploaded to the Protein Data Bank (IDs 9FLP, 9FLS, 9FLU, 9FLV, 9FLW, 9FLX, 9FLY, and 9G8B). Sequenced genomes were uploaded to the European Nucleotide Archive (PRJEB75513). This research was funded in whole or in part by the Swiss National Science Foundation (310030_212592, 315230_176189), a cOAlition S organization. The author will make the Author Accepted Manuscript (AAM) version available under a CC BY public copyright license.

SUPPLEMENTARY MATERIALS

science.org/doi/10.1126/science.adp0614
Figs. S1 to S22
Tables S1 to S10
References (*99*–*110*)
MDAR Reproducibility Checklist
Movies S1 to S9
Data S1 and S2

Submitted 6 March 2024; accepted 17 August 2024
10.1126/science.adp0614